

## Metastable Defects Decrease the Fill Factor of Solar Cells

Thomas Paul Weiss<sup>1</sup>, Omar Ramírez,<sup>1</sup> Stefan Paetel<sup>2</sup>, Wolfram Witte<sup>2</sup>, Jiro Nishinaga,<sup>3</sup>  
Thomas Feurer<sup>4</sup>, and Susanne Siebentritt<sup>1,\*</sup>

<sup>1</sup>*Department of Physics and Materials Science, University of Luxembourg, 41, rue du Brill, L-4422 Belvaux, Luxembourg*

<sup>2</sup>*Zentrum für Sonnenenergie- und Wasserstoff-Forschung Baden-Württemberg (ZSW), Meitnerstraße 1, 70563 Stuttgart, Germany*

<sup>3</sup>*Research Institute for Energy Conservation, National Institute of Advanced Industrial Science and Technology (AIST), 1-1-1 Umezono, Tsukuba, Japan*

<sup>4</sup>*Laboratory for Thin Films and Photovoltaics, Empa - Swiss Federal Laboratories for Materials Science and Technology, Überlandstraße 129, 8600 Dübendorf, Switzerland*

(Received 27 April 2022; revised 5 December 2022; accepted 10 January 2023; published 17 February 2023)

Cu(In,Ga)Se<sub>2</sub>-based solar cells exceed power conversion efficiencies of 23%. However, the fill factor of these solar cells, with best values around 80%, is relatively low (Si reaches 84.9%) mostly due to diode factors greater than 1. Recently, we proposed metastable defects, a general feature of the Cu(In,Ga)Se<sub>2</sub> alloy, to be the origin of the increased diode factor even in low injection. Here, we measure the diode factor of the bare absorber layers using excitation-dependent photoluminescence. The increased diode factor above 1 can be well described by the model of metastable defects, as well as a slight excitation dependence within the experimentally accessible range of excitation intensities. We discuss how the excitation dependence of the diode factor depends on the parameters of the metastable defects. Within the same model, we can additionally describe the experimental diode factors of *n*- and *p*-type epitaxial Cu(In,Ga)Se<sub>2</sub> films. We find that the diode factors measured optically by photoluminescence impose a lower limit for the diode factor measured electrically on a finished solar cell. Interestingly, the lowest diode factor (optical and electrical) and consequently highest fill factor of 81.0% is obtained by Ag alloying, i.e., an (Ag,Cu)(In,Ga)Se<sub>2</sub> absorber. This finding hints to a pathway to increase fill factors and thus efficiencies for Cu(In,Ga)Se<sub>2</sub>-based solar cells.

DOI: 10.1103/PhysRevApplied.19.024052

### I. INTRODUCTION

Cu(In,Ga)Se<sub>2</sub> (CIGS) is a material system used for high-efficiency thin-film photovoltaics. Record efficiencies in the laboratory have already reached 23.35% [1]. These solar cells are limited by nonradiative recombination channels [2], which have recently been linked to grain boundary recombination resulting in the hypothesis that grain size needs to be increased for higher open-circuit voltages [3]. However, apart from voltage losses, state-of-the-art CIGS solar cells also suffer from relatively low fill factors (FFs); the record CIGS solar cell has a FF of 80.4% [1] in contrast to Si with a FF of 84.9% [4,5] at similar open-circuit voltages. This FF gap can be attributed to diode factors greater

than 1 [6,7]. In fact, the diode factor of the bare absorber already exceeds the theoretical value of 1 [7–9] and thus raises the question on the origin of this loss mechanism.

We have recently shown that a metastable increase in net doping, i.e., a downshift of the majority-carrier Fermi level, upon illumination in low-injection conditions results in an increase of the diode factor. The reason is a metastable change of the net acceptor density due to injection of free electrons [10], which is a universal feature of *p*-type CIGS semiconducting alloys [11]. The metastable increase of the net acceptor density can be explained by the  $V_{\text{Se}}-V_{\text{Cu}}$  defect complex [12], which well describes many experimental observations of metastable acceptor densities such as persistent photoconductivity [7,13–15]. The defect complex involves large lattice relaxations, which can be expressed as the In-In atomic distance. For small and large In-In distances, the defect complex is in a donor and acceptor configuration, respectively. Owing to the large lattice relaxation, energy barriers are present for the transitions between donor and acceptor states [12], which is the reason for the metastability [16]. The exact nature of the

\*susanne.siebentritt@uni.lu

Published by the American Physical Society under the terms of the [Creative Commons Attribution 4.0 International license](#). Further distribution of this work must maintain attribution to the author(s) and the published article's title, journal citation, and DOI.

metastable defect is not critical here. We use a model of a metastable defect that is in a donor state in equilibrium in a *p*-type material and changes to an acceptor state upon electron injection.

Notably, metastable defects due to large lattice relaxations are generally found in semiconducting materials (see, e.g., Ref. [16] and references therein). Other industrially used photovoltaic absorber materials have been demonstrated to exhibit metastable defect behavior, e.g., Si [17] and CdTe [18]. In addition, novel material systems generally exhibit lower structural symmetries than cubic symmetry and are thus more prone to the formation of metastable defects [19]. Thus, while we use here the specific properties of the  $V_{\text{Se}}\text{-}V_{\text{Cu}}$  defect complex in *p*-type CIGS, the model can be applied to other systems as well. Furthermore, the diode factor, which we demonstrate is influenced by metastabilities, is important in other (opto)electronic applications, not just solar cells.

In Ref. [7] we used the model of such a metastable defect to explain the increased diode factor above 1, which directly results in reduced FFs. Owing to the direct impact of the metastability on device performance, it is of major importance to scrutinize the model's capability to correctly describe experimental data. In particular, in Ref. [7] the simulated diode factor shows a strong dependence with respect to the excitation level within the model of metastable defects, i.e., it depends on the density of injected minority carriers (electrons for *p*-type CIGS). In contrast, the diode factor measured experimentally, as also presented in this manuscript, is not strongly excitation dependent. The simulated behavior of the diode factor with excitation depends strongly on the exact parameters of the metastable defect transitions. Therefore, the question arises about whether it is possible to find reasonable parameters that can explain an almost constant diode factor above 1 over the experimentally accessible range of excitations. We discuss in the following how the model depends on the properties of the metastable defect, and demonstrate that it is, in fact, able to describe an almost excitation-independent diode factor in the range of experimentally accessible excitations. In addition, the weak excitation dependence of the diode factor observed in experiments on CIGS absorbers is shown to be well described by the model.

The paper is structured as follows. First, the theoretical background of the metastable defect model is elaborated. We demonstrate how the parameters of the metastable defect influence the excitation dependence of the diode factor. Next, we investigate epitaxial CIGS films, which are known to exist as *n*-type or *p*-type semiconducting layers [20,21]. The results give additional support for the model of the increased diode factor being due to a metastable defect, which is a donor in the *p*-type material in equilibrium and turns into an acceptor upon electron

injection—or is already an acceptor in equilibrium in the *n*-type material. Finally, diode factors are measured optically on various high-efficiency CIGS samples from different laboratories. These samples show very different diode factors, which can be reproduced by the model with reasonable values for the parameters of the metastable defect. Also, the weak excitation dependence of the diode factor is fitted by the model with, in general, good agreement. A comparison with a large set of solar cells from several different institutes shows that the FF, and consequently the efficiency, is limited by the diode factor of state-of-the-art devices.

## II. THEORETICAL BACKGROUND

As shown previously, the diode factor  $A$  of the bare absorber can be measured and simulated using intensity-dependent photoluminescence (PL) [8,22] as

$$A = \frac{\partial \ln Y_{\text{PL}}}{\partial \ln G}, \quad (1)$$

where  $Y_{\text{PL}}$  is the integrated PL flux (measured or simulated, see Sec. III for details) and  $G$  the generation flux [7,8,22]. Another way of looking at Eq. (1) is by noting that the PL flux is proportional to  $\exp(\Delta\mu/k_B T)$ , where  $\Delta\mu$  is the quasi-Fermi-level splitting  $k_B$  the Boltzmann constant and  $T$  the temperature [23]. Thus, the diode factor in Eq. (1) can equally be written as

$$A = \frac{\partial \Delta\mu}{\partial \ln G} \quad (2)$$

and is represented as the shift of the quasi-Fermi-levels with respect to the generation flux. Experimentally, Eq. (1) offers the advantage that  $A$  can be measured without an absolute calibration of the PL flux.

CIGS is a *p*-type absorber layer with dominating Shockley-Read-Hall (SRH) recombination, which is operated in low-injection conditions during our PL measurements. Therefore, a diode factor of 1 is expected, as only the electron Fermi level is expected to move upon illumination [7,24]. Recently, we have shown that a diode factor above 1 can be explained by an additional downshift of the hole quasi-Fermi-level upon illumination, which happens even in low-injection conditions [7]. We have shown that the downshift of the hole (majority) quasi-Fermi-level can be described by metastable defects involving large lattice relaxations [7]. In CIGS, the  $V_{\text{Cu}}\text{-}V_{\text{Se}}$  divacancy complex is such a defect [12], which has a donor and an acceptor state. The transition rates from acceptor to donor  $U_{A \rightarrow D}$  and from donor to acceptor  $U_{D \rightarrow A}$  are given by [14]

$$\begin{aligned} U_{A \rightarrow D} &= f_A (\tau_{EE}^{-1} + \tau_{HC}^{-1}) N_{MS} \\ U_{D \rightarrow A} &= (1 - f_A) (\tau_{HE}^{-1} + \tau_{EC}^{-1}) N_{MS} \end{aligned} \quad (3)$$

In Eq. (3), the  $\tau_{ij}^{-1}$  describe the rate constants for the most probable transitions [12] for the conversion between the donor and the acceptor state, with  $i = E$  or  $H$  abbreviating electron or hole, and  $j = E$  or  $C$  abbreviating emission or capture, and  $N_{MS}$  is the density of metastable defects. The ratio of metastable defects in the acceptor state, acceptor occupation, is denoted by  $f_A$  and is given by [14]

$$f_A = \frac{\tau_{HE}^{-1} + \tau_{EC}^{-1}}{\tau_{HE}^{-1} + \tau_{EC}^{-1} + \tau_{EE}^{-1} + \tau_{HC}^{-1}}. \quad (4)$$

Each transition process with the rate constant  $\tau_{ij}^{-1}$  involves two charge carriers. In addition, a potential barrier  $\Delta E_{ij}$  is present due to the large changes of the In-In bonding

distance [12]. This potential barrier enters as a Boltzmann term into the rate constants. Thus, in the case of insufficient thermal energy, the defect can be in a metastable state. Expressions for  $\tau_{ij}^{-1}$  and their transition processes are summarized in Table I. The ratio of metastable defects in the donor state is given by  $1 - f_A$ . We should note that we use the  $V_{Se}$ - $V_{Cu}$  divacancy for a  $p$ -type CIGS absorber as the model for the metastable defect. However, any metastable defect has a forward and a backward reaction governed by rate constants and activation energies. Thus, the model is not specific to the  $V_{Se}$ - $V_{Cu}$  divacancy.

Using the expressions for the transition rates  $\tau_{ij}^{-1}, f_A$  in Eq. (4) can be expressed as

$$f_A = \frac{N_V^2 \exp\left(-\frac{\Delta E_{HE}}{k_B T}\right) + n N_V \exp\left(-\frac{\Delta E_{EC}}{k_B T}\right)}{N_V^2 \exp\left(-\frac{\Delta E_{HE}}{k_B T}\right) + n N_V \exp\left(-\frac{\Delta E_{EC}}{k_B T}\right) + p N_C \exp\left(-\frac{\Delta E_{EE}}{k_B T}\right) + p^2 \exp\left(-\frac{\Delta E_{HC}}{k_B T}\right)}. \quad (5)$$

where  $N_V$  and  $N_C$  denote the effective density of states in the valence and conduction band, respectively. From Eq. (5) it becomes obvious that the acceptor occupation depends on the minority-carrier density and therefore on the excitation conditions, i.e., the generation flux  $G$ . In low-injection conditions and with reasonably good transport properties (flat quasi-Fermi-levels), the minority-carrier density  $n$  is given by

$$n \approx G \tau_n / d, \quad (6)$$

where  $\tau_n$  denotes the minority-carrier lifetime and  $d$  the absorber thickness. It is noted that in Eq. (6) the generation flux is given per unit area and unit time (e.g.,  $\text{cm}^{-2} \text{s}^{-1}$ ). In particular,  $G$  is not a rate (e.g., units of  $\text{cm}^{-3} \text{s}^{-1}$ ) and therefore the thickness  $d$  needs to be considered to obtain the excess charge carrier density. The hole density in Eq. (5) is given in the low-injection case by  $p \approx N_A + f_A N_{MS} - (1 - f_A) N_{MS}$ , which is the fixed (nonmetastable) acceptor density  $N_A$  plus the metastable defects in the acceptor configuration  $f_A N_{MS}$  minus the metastable defects in the donor configuration  $(1 - f_A) N_{MS}$ . Finally, the diode factor can be calculated as follows (see Ref. [7] for details):

(1) Determine the quasi-Fermi-levels  $E_{Fn}$  and  $E_{Fp}$  for electrons and holes, respectively, using the charge neutrality condition and the condition that generation equals recombination in steady state. Equation (5) is taken into account and solved self consistently, i.e., the occupation of the metastable defect is respected. The process for the calculation and the model of the semiconductor are illustrated in Fig. 1.

(2) Calculate the quasi-Fermi-level splitting  $\Delta\mu = E_{Fn} - E_{Fp}$  as a function of the generation flux, i.e., the process described under (1) is repeated for various values of  $G$ . The PL flux is obtained according to Planck's generalized law [23]. It is noted that only the relative PL is calculated according to  $Y_{PL} \propto \exp(\Delta\mu/k_B T)$ . This expression is sufficient here as we only compare the resulting diode factors given by Eq. (1). In Equation (1), any proportionality factor drops out due to the derivative of the logarithm.

(3) Calculate the diode factor using Eq. (1). It is noted that the diode factor can also be derived directly via Eq. (2) using the dependence of  $\Delta\mu$  as a function of the generation flux. However, we calculate  $Y_{PL}$  as well, as this quantity can easily be obtained experimentally.

The simulations in Fig. 2 exemplify the physical meaning of a diode factor greater than 1 due to metastable defects in a  $p$ -type absorber layer. (Further details of Fig. 2 are discussed in the following.) With increasing generation flux,  $E_{Fn}$  increases as expected from Eq. (6). In the case of SRH recombination without metastable defects,  $E_{Fp}$  is constant [purple dash dotted line labeled "only SRH" in Fig. 2(a)] and the shift of  $E_{Fn}$  results in  $A = 1$ . However, with the involvement of metastable defects,  $E_{Fp}$  shifts towards the valence band due to their conversion from donor to acceptor state. This additional shift results in  $A > 1$ . The calculated relative PL fluxes are shown in Fig. 2(b). The derivative in a double-logarithmic plot [Eq. (1)] gives the diode factors shown in Fig. 2(c).

TABLE I. Summary of the dominating processes governing the transition of the metastable defect with large lattice relaxations. Here, the expressions are explicitly written for the  $V_{\text{Se}}\text{-}V_{\text{Cu}}$  divacancy defect in CIGS;  $\nu_{\text{ph}}$  is the phonon frequency, and  $c_n$  and  $c_p$  the capture constants for electrons and holes, respectively.

Rate constant	Process name	Process description	Expression	Transition process
$\tau_{EC}^{-1}$	Electron capture	Electron capture + hole emission	$\tau_{EC}^{-1} = \frac{1}{\nu_{\text{ph}}} c_n c_p n N_V \exp\left(-\frac{\Delta E_{EC}}{k_B T}\right)$	Donor $\rightarrow$ Acceptor
$\tau_{EE}^{-1}$	Electron emission	Electron emission + hole capture	$\tau_{EE}^{-1} = \frac{1}{\nu_{\text{ph}}} c_n c_p p N_C \exp\left(-\frac{\Delta E_{EE}}{k_B T}\right)$	Acceptor $\rightarrow$ Donor
$\tau_{HC}^{-1}$	Hole capture	Double hole capture	$\tau_{HC}^{-1} = \frac{1}{\nu_{\text{ph}}} c_p^2 p^2 \exp\left(-\frac{\Delta E_{HC}}{k_B T}\right)$	Acceptor $\rightarrow$ Donor
$\tau_{HE}^{-1}$	Hole emission	Double hole emission	$\tau_{HE}^{-1} = \frac{1}{\nu_{\text{ph}}} c_p^2 N_V^2 \exp\left(-\frac{\Delta E_{HE}}{k_B T}\right)$	Donor $\rightarrow$ Acceptor

Experimentally, as shown in Fig. 2(c), the diode factor can be determined from the measured PL flux as a function of the generation flux, as in Eq. (1). However, these data are rather noisy, see, e.g., Fig. 4(b) below. Therefore, the experimental diode factor is often not determined differentially according to Eq. (1), i.e., as a function of the generation flux, but from a straight line fit in a double-logarithmic plot, see, e.g., Refs. [7,8,24,25]. Using such a linear fit instead of Eq. (1) directly assumes a generation-independent diode factor. However, upon closer inspection, the PL flux generally has a slight negative curvature with respect to the generation flux [7]. For the CIGS samples studied here, this is evidenced by the U-shaped residuals of the experimental PL flux and a straight line fit (Appendix A).

As shown in Sec. III, high-quality CIGS absorbers exhibit a diode factor greater than 1 with a small or sometimes no generation flux dependence. We demonstrate in Sec. IV B that these experimental findings can be described by the model presented here. Before we get to this point, we want to explore the capabilities of the metastable defect model and how a diode factor greater than 1 and *almost* generation flux independent (over several orders of

magnitude) can be described as functions of the properties of the metastable defect. The relevance of this study is that it describes the landscape of the parameters of the metastable defect and how they influence the diode factor. In that sense, a closer inspection of the generation flux dependence of the diode factor in the context of metastable defect behavior might also be interesting for other material systems, as, for example, observed in perovskites [26] or CdTe [27].

We utilize a fitting routine to determine the parameters of the metastable defects in order to obtain an approximately constant diode factor for generation fluxes between  $10^{13}$  and  $10^{17} \text{ cm}^{-2} \text{ s}^{-1}$ . This range describes the experimentally accessible values to measure the PL flux (and thus the diode factor). The fitting routine is a least-squares fit reducing the squared residuals  $X^2$  of the calculated diode factors  $A_{\text{calc}}^i$  and a constant value  $A_{\text{fix}}$  [see Fig. 2(c)] at predefined generation fluxes  $G^i$ . Thus, the function to minimize is expressed as

$$X^2 = \frac{1}{N} \sum_i [(A_{\text{exp}}^i - A_{\text{calc}}^i)]^2, \quad (7)$$

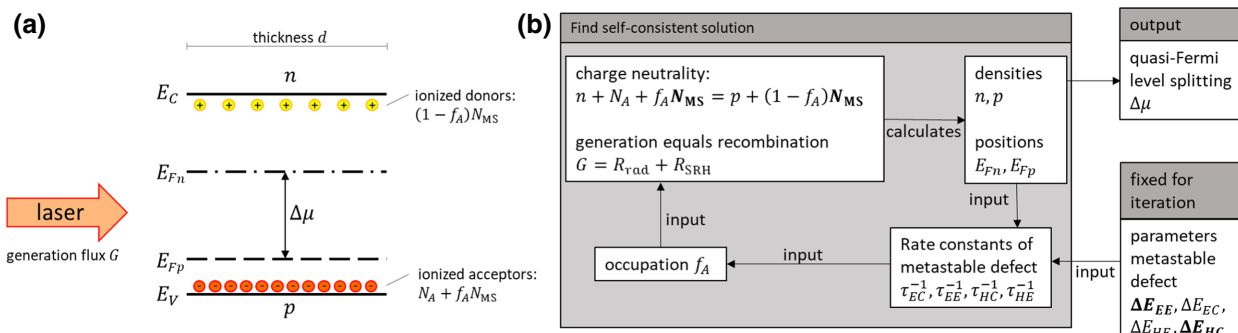


FIG. 1. (a) Model for the calculation of the quasi-Fermi-level splitting  $\Delta\mu$  (and thus the PL flux) as a function of the generation flux  $G$ . A homogeneous  $p$ -type absorber with a fixed (nonmetastable) doping density of  $N_A$  is assumed without surface recombination. A metastable defect with density  $N_{\text{MS}}$  as defined in Table I is included, which can exist in a donor or acceptor configuration. (b) Illustration of the calculation of the quasi-Fermi-level splitting incorporating a metastable defect. The photogenerated electrons and holes influence the occupation of the metastable defect  $f_A$  via Eq. (5). As a result, the condition for the charge neutrality changes as well as the recombination rates. A self-consistent solution is found if the relative change in the charge densities and recombination rates are below a threshold value  $\epsilon$ . From the positions of the quasi-Fermi-levels  $E_{Fn}$  and  $E_{fp}$ , the quasi-Fermi-level splitting  $\Delta\mu$  is calculated. To calculate the diode factor,  $\Delta\mu$  is calculated as a function of the generation flux.

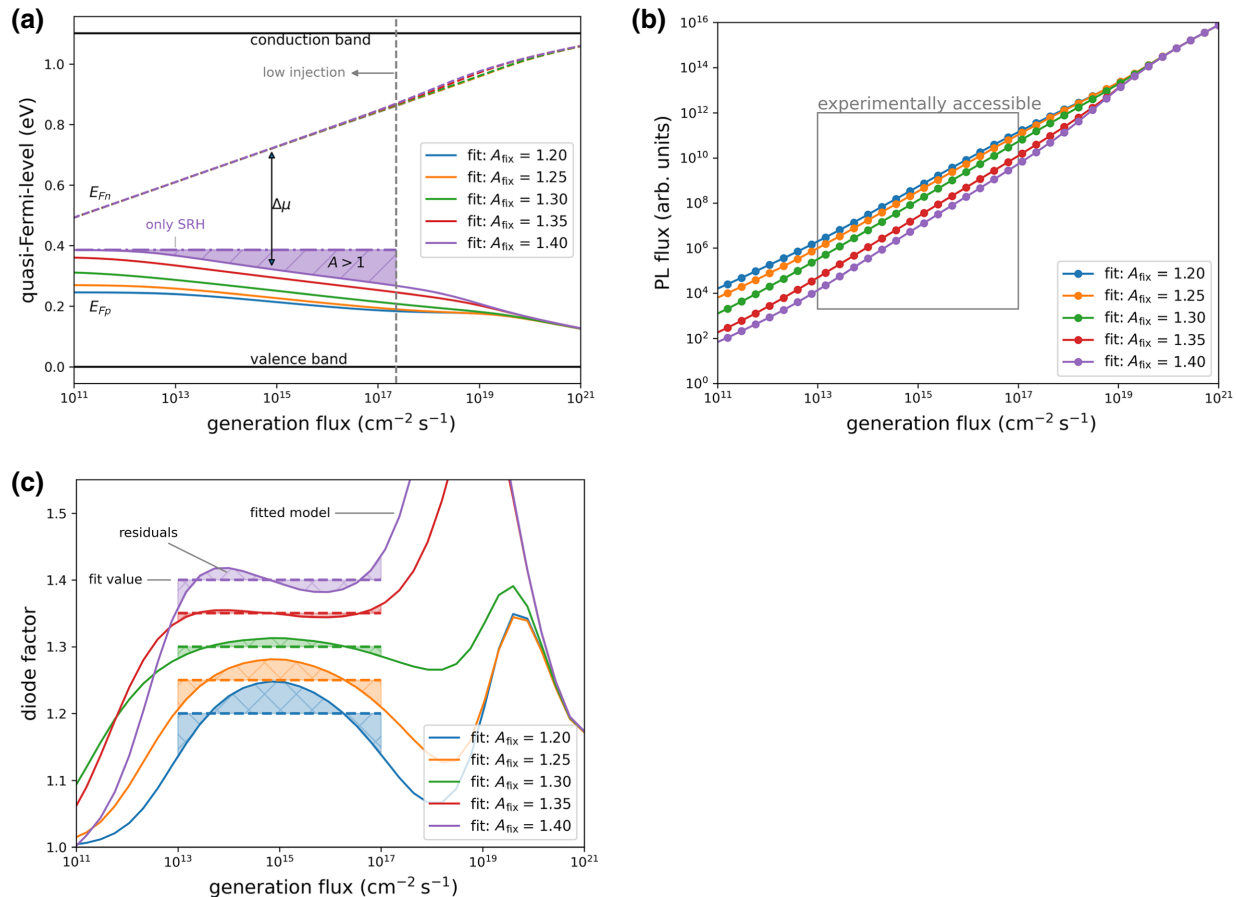


FIG. 2. Diode factor fits for various values  $A_{\text{fit}}$  of diode factors constant within the experimentally accessible range of generation fluxes [dashed horizontal lines in (c)]. Fit parameters are the activation energies and density of the metastable defect transitions. (a) Calculated electron and hole quasi-Fermi-levels for a semiconducting thin film including metastable defects. Owing to the conversion of metastable defects from donor to acceptor configuration, the hole quasi-Fermi-level shifts towards the valence band even in low-injection conditions (purple shaded area for the curve labeled  $A = 1.40$ ). (b) Calculated relative PL flux based on the quasi-Fermi-level splitting  $\Delta\mu$  from (a). (c) Calculated diode factor as a function of the generation flux using Eq. (1). Activation energies and density of the metastable defect are determined by a fitting routine, which reduces the squared residuals (shaded areas) between the calculated diode factors (solid line) and a constant value (horizontal dashed lines). Other parameters are given in Table III.

where  $N$  is the number of generation fluxes within a certain interval. Here, we use  $N = 9$  equidistant generation fluxes on a logarithmic scale between  $10^{13}$  and  $10^{17} \text{ cm}^{-2} \text{s}^{-1}$ . Thus, for each iteration of the fitting procedure, the quasi-Fermi-level splitting is calculated as a function of the generation flux from which the diode factor (as a function of the generation flux) is calculated, as described previously.

Prior to simply applying the process flow shown in Fig. 1, which is needed for the calculation of the quasi-Fermi-level splitting and thus for the fitting of the diode factor, the following considerations and parameter choices are made, which facilitate the fitting routine by reducing the number of free parameters.

(a) The band gap  $E_g$  and the Fermi level dictate the equilibrium densities  $n_0$  and  $p_0$  of free carriers in the

conduction and valence band, respectively, and in turn define the equilibrium occupation  $f_A$  via Eq. (5). The position of the electron Fermi level, where  $f_A = 0.5$ , is defined as the charge transition level  $E_{\text{tr}}$ . From detailed balance considerations,  $E_g$ ,  $E_{\text{tr}}$ , and the four  $\Delta E_{ij}$  are not independent from each other but obey the following two relations [14]:

$$E_{\text{tr}} = \frac{1}{2}(E_g + \Delta E_{EC} - \Delta E_{EE}), \quad (8)$$

$$E_{\text{tr}} = \frac{1}{2}(\Delta E_{HE} - \Delta E_{HC}). \quad (9)$$

(b) Here, zero energy is set to  $E_V = 0$ . In the following discussion and simulations,  $E_g$  is fixed to 1.1 eV. Then,  $E_{\text{tr}}$  and  $\Delta E_{HE}$  are calculated via Eqs. (8) and (9), respectively, by using the remaining three free parameters  $\Delta E_{EC}$ ,  $\Delta E_{EE}$ , and  $\Delta E_{HC}$ .

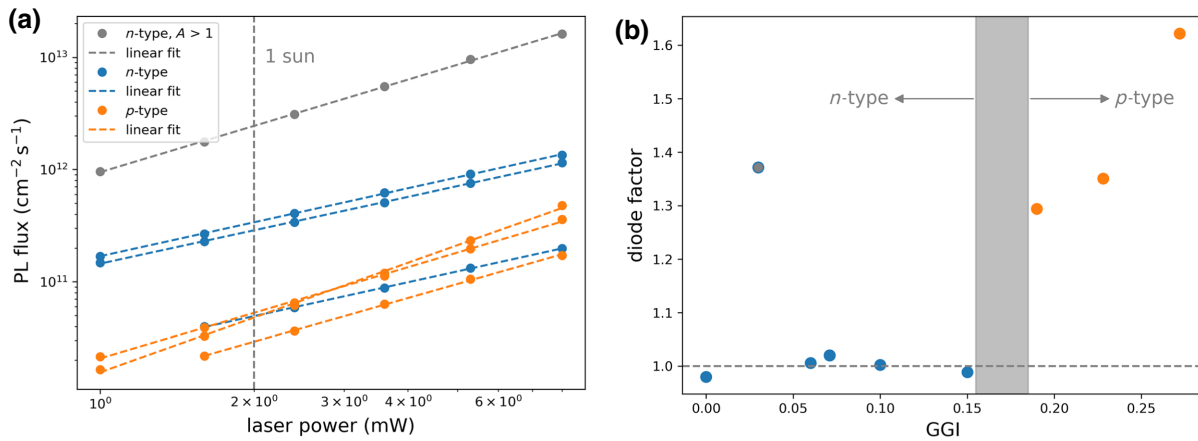


FIG. 3. (a) Measured and spectrally integrated PL flux for epitaxial CIGS absorbers with different GGI values. A linear fit is applied to determine the diode factor from the slope. (b) Diode factor versus the GGI. A transition from  $A = 1$  to  $A > 1$  is observed where the semiconductor turns from *n*-type to *p*-type [21]. The sample in gray is *n*-type but shows strong contributions from secondary phases in the Raman spectrum.

(c) From Eq. (5) it is obvious that the occupation  $f_A$  does not depend on the absolute values of  $\Delta E_{ij}$ , i.e.,  $f_A$  is invariant upon shifting all  $\Delta E_{ij}$  by the same constant  $\Delta E$ . This additional degree of freedom allows us to fix one of the remaining energy barriers ( $\Delta E_{EC}$ ,  $\Delta E_{EE}$ , and  $\Delta E_{HC}$ ). While this procedure does not change  $f_A$ , it implies certain dynamics of the metastable defect. However, the dynamics are not part of the present paper. Consequently, if not mentioned otherwise, we fix  $\Delta E_{EC} = 0.35$  eV without loss of generality.

(d) The nonmetastable doping density  $N_A$  is fixed to  $10^{16} \text{ cm}^{-3}$ , while the density of metastable defects  $N_{MS}$  is allowed to vary during the fitting of the diode factor. Similar simulation results are obtained

for fixed doping densities, for instance, at  $10^{17} \text{ cm}^{-3}$  (Appendix B), as it is the difference between the doping density and metastable defect density that is mainly of importance [7].

The free parameters, which are used for the fitting of the diode factor, are highlighted in a bold font in Fig. 1. Other (fixed) parameters for the calculations are the effective density of states in the conduction and valence bands of  $N_C = 7.8 \times 10^{17} \text{ cm}^{-3}$ ,  $N_V = 2.1 \times 10^{19} \text{ cm}^{-3}$  (corresponding to effective masses for electrons and holes of  $m_e^* = 0.1 m_e$  and  $m_h^* = 0.9 m_e$ , respectively). For radiative recombination, the radiative recombination constant is set

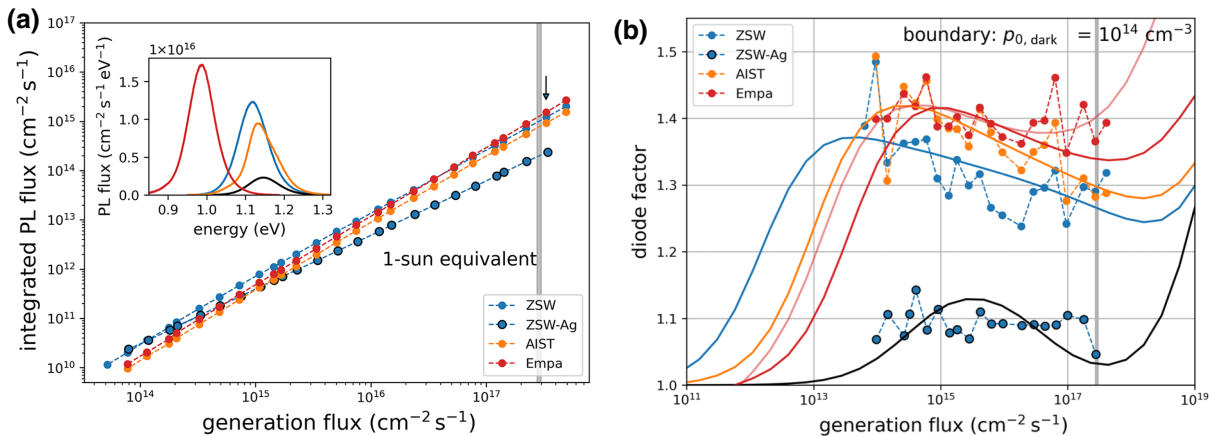


FIG. 4. (a) Experimentally measured spectrally integrated PL flux as a function of the generation flux for four polycrystalline  $\text{Cu}(\text{In},\text{Ga})\text{Se}_2$  absorber layers. Gray vertical bar indicates a 1-sun equivalent generation flux. Inset shows measured PL spectra at equivalent generation fluxes just above 1-sun (black arrow). (b) Extracted differential diode factor according to Eq. (1) (filled symbols). Solid (dark) lines represent best fits following the model of metastable defects with the boundary condition of a minimum free-hole density of  $10^{14} \text{ cm}^{-3}$ . Data from the Empa sample are the only case where a significantly better fit is obtained by loosening the boundary condition to  $p_{0,\text{bound}} = 10^{13} \text{ cm}^{-3}$  (light red curve).

TABLE II. Fitted parameters for the metastable defects to describe the generation flux dependence of the diode factor shown in Figs. 2(c) and 4(b). The barrier for the electron capture is set constant to  $\Delta E_{EC} = 0.35$  eV and the fixed doping density to  $N_A = 10^{16}$  cm<sup>-3</sup>. The experimental data shown in Fig. 4(b) are fitted with the boundary condition of a free-hole density of  $p_{0,\text{bound}} = 10^{14}$  cm<sup>-3</sup>. For the Empa sample only a significantly better fit is obtained with the relaxed boundary condition of  $p_{0,\text{bound}} = 10^{13}$  cm<sup>-3</sup> and thus these values are given here as well.

Sample	$\Delta E_{HC}$ (eV)	$\Delta E_{EE}$ (eV)	$N_{MS}$ (cm <sup>-3</sup> )
Figure 2(a) (fit to constant diode factor)			
$A = 1.20$	0.319	0.696	$8.610 \times 10^{15}$
$A = 1.25$	0.278	0.654	$9.462 \times 10^{15}$
$A = 1.30$	0.205	0.581	$9.908 \times 10^{15}$
$A = 1.35$	0.082	0.354	$9.977 \times 10^{15}$
$A = 1.40$	0.013	0.534	$1.007 \times 10^{16}$
Figure 4(b) (fit to experimental data with $p_{0,\text{bound}} = 10^{14}$ cm <sup>-3</sup> )			
ZSW	$0.22 \pm 0.02$	$0.73 \pm 0.19$	$10^{16.014 \pm 0.016}$
ZSW-Ag	$0.34 \pm 0.01$	$> 0.75$	$10^{15.6 \pm 1.5}$
AIST	$0.20 \pm 0.03$	$0.76 \pm 0.06$	$10^{16.06 \pm 0.04}$
Empa	$0.17 \pm 0.03$	$0.66 \pm 0.03$	$10^{16.05 \pm 0.03}$
Empa ( $p_{0,\text{bound}} = 10^{13}$ cm <sup>-3</sup> )	$0.09 \pm 0.02$	$0.56 \pm 0.03$	$10^{16.013 \pm 0.005}$

to  $B = 1.28 \times 10^{-10}$  cm<sup>-3</sup>s<sup>-1</sup>. For SRH recombination, a mid-gap defect state is assumed with an equal lifetime for electrons and holes of 100 ns.

To check the validity of the simulations, the transition rates from acceptor to donor  $U_{A \rightarrow D}$  and from donor to acceptor  $U_{D \rightarrow A}$  are calculated according to Eq. (3). For the solution at steady state, these rates must be equal (see Appendix C).

Figure 2(c) shows the simulations (solid lines), where the diode factor is fitted to various generation-flux-independent diode factors between 1.2 and 1.4. The fitted parameters for the metastable defect are listed in Table II. As described previously, the reason for diode factors above 1 is the downshift of the hole quasi-Fermi-level, as shown in Fig. 2(a), as a consequence of the conversion of metastable defects from donor to acceptor state. It is noted that low-injection conditions prevail in these simulations (Appendix D) for generation fluxes below (in the worst case) approximately  $3 \times 10^{17}$  cm<sup>-2</sup>s<sup>-1</sup>.

It is interesting to note that the best fitting results are obtained for diode factors between 1.30 and 1.35. For smaller diode factors, the generation flux dependence becomes stronger within the model of one metastable defect. Appendix E gives further details concerning the dependence of the rate constants  $\tau_{ij}^{-1}$  as a function of the free-carrier densities, which change as a function of the generation flux.

### III. EXPERIMENT

To examine the theoretical model of metastable defects introduced in Ref. [7] and elaborated previously, epitaxial

and polycrystalline CIGS films are investigated. The epitaxial films under investigation here have neither grain boundaries nor extrinsically added doping, such as alkalis. Thus, the CIGS bulk properties are explored. High-quality polycrystalline CIGS films are used to examine the metastable defect model by measurements of the diode factor on a sufficiently wide range of generation fluxes. In addition, the relevance of the diode factor on the FF and the efficiency of finished solar cells is demonstrated.

Epitaxial Cu(In,Ga)Se<sub>2</sub> absorbers with thicknesses around 600 nm are grown by metalorganic vapor phase epitaxy on (100)-oriented undoped GaAs substrates at 520 °C. In order to tune the Ga content, a two-step growth process is implemented. First, a Cu(In,Ga)Se<sub>2</sub> layer with [Ga] : ([Ga] + [In]) (GGI) ratio of 0.4 is grown, followed by a layer of pure CuInSe<sub>2</sub>. By adjusting the thickness of the first and second layers, precise control of the integral Ga content of the final CIGS layer can be achieved. All samples have a [Cu] : ([Ga] + [In]) ratio between 0.83 and 0.89 (Cu-poor), which is a necessary condition to obtain *n*-type conductivity in CuInSe<sub>2</sub> [28]. Details of the sample's growth and the dependency of the conduction type (*n*-type or *p*-type) on the gallium content can be found in Ref. [21]. In particular, for compositional ratios of GGI  $\geq 0.19$ , *p*-type conduction is observed, while for GGI  $\leq 0.15$ , *n*-type conduction is obtained [21].

Polycrystalline CIGS absorber layers and their respective solar cell devices are grown by ZSW, AIST, and Empa. The absorber layers are grown following a three-stage or modified three-stage coevaporation process [29,30] from elemental evaporation sources. The deposition process results in a double-graded compositional profile such that the Ga concentration has a minimum within the bulk of the absorber layer. As a result, the band gap is graded with a minimum corresponding to the minimum Ga concentration. Additional details concerning the growth process are given in the following.

(a) ZSW A Mo-coated soda-lime glass serves as a substrate providing Na and some K by diffusion into the CIGS layer at elevated temperatures. Absorber layers are grown in a 30 × 30 cm<sup>2</sup> inline deposition machine with a multistage coevaporation process. For some absorber layers, Ag is also coevaporated. At the end of the CIGS process, an *in situ* RbF postdeposition treatment (PDT) is carried out under a Se atmosphere [31,32]. Solar cells are finished using a solution-grown CdS buffer layer, a sputtered ZnO/Al-ZnO double-window layer and a Ni/Al contact grid. Individual solar cells are scribed mechanically with an area of 0.5 cm<sup>2</sup>. Solar cells yield efficiencies of around 18.5% (total area, without antireflective coating). The PL peak position, representative of the band-gap minimum [33], is around 1.10–1.15 eV. In total, solar cells from 14 different deposition runs are evaluated. From each sample, ten solar cells are manufactured. For the analysis of the

current-voltage characteristics of the solar cells, only those solar cells are taken into account where efficiencies deviate less than 1% absolute from the highest efficiency for each sample.

(b) *AIST* The CIGS absorber layer is grown by a static multistage coevaporation process. At the end of the process a KF PDT is carried out *in situ*, and the solar cells are finished using a CdS buffer layer, a sputtered ZnO/Al-ZnO window layer, and Ni/Al contact grid [34]. The solar cell yields an efficiency of 21.6% (with antireflective coating). The PL peak position is around 1.13 eV.

(c) *Empa* The CIGS absorber layer is grown by a static multistage coevaporation process, where Ga is supplied only during the first stage [35]. A RbF PDT is carried out *in situ* and the solar cell yields an efficiency of 19.2% (with antireflective coating), which is the same device as published elsewhere [36]. The Ga is located only towards the back contact for passivation purposes [35] and the PL peak position is at 1.0 eV, which corresponds to a CuInSe<sub>2</sub> stoichiometry with GGI = 0.

Experimentally, the differential diode factor is measured by intensity-dependent PL spectroscopy using Eq. (1). Illumination is provided by a 660-nm-wavelength diode laser. The intensity of the laser beam is varied by the output power of the laser as well as by optical density (OD) filters. The generation flux is calibrated at the sample position, from where the PL light is collected. First, a power meter measures the power of the total beam area, and second, a camera captures the beam shape to determine the spot size (approximately 1.1-mm radius). Subsequently, the power is calculated in the center of the Gaussian spot, from where the PL is collected.

Polycrystalline CIGS absorbers have a sufficiently high PL flux to allow the reduction of the generation flux by several orders of magnitude below 1-sun excitation, which corresponds to the same absorbed photon flux as realized by illumination with an AM1.5G spectrum. Thus, it is reasonable to evaluate the differential diode factor according to Eq. (1). To reduce the noise in the diode factor when calculating the derivative, it proves to be important to reduce statistical errors for the determination of the generation flux as much as possible. Therefore, the calibration mentioned previously (power and beam spot size measurement) is carried out for each setting of laser output power and OD filter. Additionally, a CdS buffer layer is deposited on the front surface for passivation purposes and to prevent degradation during PL measurements [37,38]. For the samples without the addition of Ag, i.e., the samples from Empa, AIST, and ZSW without Ag, the processing after the CdS layer is omitted, i.e., no transparent conductive oxide is deposited. For the sample including Ag during the deposition, the absorber is only available in the form of a finished solar cell device. For the PL study, the absorber is then etched in acetic acid (AcOH), which is known to

remove the window layers but not the CdS buffer layer [39]. Here, the sample is etched in 5% AcOH for 1 min in an ultrasonic bath. The removal of ZnO and the presence of CdS after the etching is checked by energy dispersive x-ray spectroscopy (Appendix F).

The generation flux dependence of the diode factor for the polycrystalline CIGS samples is fitted with the model of metastable defects. However, the model is not fitted to a constant diode factor value as described in Sec. II. Instead, the residuals are calculated from the difference of the calculated diode factors  $A_{\text{calc}}^i$  of the model and the experimental diode factors  $A_{\text{exp}}^i$  measured at each generation flux  $G_{\text{exp}}^i$ . Both  $A_{\text{calc}}^i$  and  $A_{\text{exp}}^i$  are only weakly generation dependent in the range of generation fluxes accessible experimentally. With free fitting, the dark hole concentration tends to be very low. Therefore, boundary conditions forcing a free-hole density  $p_0$  in the dark (i.e., the lowest generation fluxes) greater than  $p_{0,\text{bound}}$  are applied to several fits. The boundary conditions are implemented in the fitting routine as a “soft” bound so that the residuals are scaled by a factor  $f_{\text{bound}}$  defined as

$$f_{\text{bound}} = \begin{cases} 1 + \log_{10}(p_0) - \log_{10}(p_{0,\text{bound}}) & \text{for } p_0 > p_{0,\text{bound}} \\ 1 & \text{otherwise} \end{cases} \quad (10)$$

Thus, the following expression is minimized:

$$X^2 = \frac{1}{N} \sum_i [f_{\text{bound}}(A_{\text{exp}}^i - A_{\text{calc}}^i)]^2, \quad (11)$$

where, in this case,  $N$  is the number of experimentally determined differential diode factors. Errors of the fitting parameters are calculated from the covariance matrix of the fit result.

Epitaxial films have a lower PL flux compared to polycrystalline films for several reasons:

(i) Epitaxial absorber layers are not doped by alkali elements and thus possess a low net doping density. For polycrystalline films without the addition of alkalis, low doping densities of the order of  $10^{14} \text{ cm}^{-3}$  are measured [40,41]. Similar doping densities are estimated for the epitaxial *p*-type CIGS films studied here [21]. As the radiative recombination rate is directly proportional to the doping density in low-injection conditions, the PL flux is accordingly small. In contrast, with the addition of alkalis, doping densities of the order of  $10^{16} \text{ cm}^{-3}$  are possible for polycrystalline films [40,41]. Alkali doping increases the PL flux of epitaxial films as well [42].

(ii) The epitaxial films studied here are rather thin, and thus surface recombination has a stronger impact on the carrier recombination dynamics [43]. In particular, electron mobilities can reach values up to  $1000 \text{ cm}^2 \text{ V}^{-1} \text{ s}^{-1}$  in

epitaxial CIGS films [44], which will further enhance surface recombination. It is noted that surface recombination is not included in the model described in Sec. II. However, surface recombination lowers the concentration of excess charge carriers in the bulk and can thus be described by an effective bulk lifetime, which is smaller than the SRH lifetime [43]. Apart from that, Wang *et al.* showed by simulation and experiment that the increased effective doping density due to metastable defects can lead to increased back surface recombination as, in general, non-flat-band conditions prevail [9]. This effect lowers the diode factor and weakens the excitation dependence.

In consequence, even though bulk defect properties might be similar to or even better than those for polycrystalline films, the PL flux has always been observed to be much lower for undoped epitaxial films. Therefore, the intensity could be varied by roughly only 1 order of magnitude (from about 1/2 to 4 sun excitation). In that case, the diode factor is extracted from a linear fit. As shown in the following, the diode factor varies only weakly with generation flux. Thus, the linear fit gives a good estimate for this range of generation fluxes. Measurements are carried out without a CdS buffer layer. Instead, the samples are measured in a N<sub>2</sub> atmosphere to prevent degradation.

Raman spectra are recorded at room temperature with a 532-nm laser using a 50× objective lens and a numerical aperture of 0.5 in combination with a 2400-line/mm grating. A filter is used to block the incident laser beam.

Current density versus voltage (*J-V*) characteristics are measured in the respective institutes of device fabrication under standard test conditions. A fitting routine based on a one-diode model [Eq. (12)] is used for the illuminated *J-V* characteristics to extract diode parameters.

$$J(V) = J_0 \left[ \exp \left( \frac{q(V - r_s J)}{A_{\text{el}} k_B T} \right) - 1 \right] + \frac{V - r_s J}{R_{\text{sh}}} + J_{\text{ph}}, \quad (12)$$

where  $J_0$  is the saturation current density,  $A_{\text{el}}$  the electrical diode factor,  $r_s$  the series resistance,  $R_{\text{sh}}$  the shunt resistance, and  $J_{\text{ph}}$  the photocurrent. In the one-diode model, in general, the photocurrent is determined as  $J_{\text{ph}} = J_{\text{SC}}(1 + r_s/R_{\text{sh}})$ , where  $J_{\text{SC}} = J(0)$  is the short-circuit current density. For the solar cells investigated here it holds that  $r_s \ll R_{\text{sh}}$  and thus  $J_{\text{ph}} \approx J_{\text{SC}}$ . The one-diode fit is subsequently carried out for the data  $J(V) - J_{\text{SC}}$ , which proves to be much more robust than having  $J_{\text{ph}}$  as an additional fit parameter. Two fitting routines are used: (i) the “iv-fit” routine [45] and (ii) a self-implemented fitting routine using an orthogonal distance regression with logarithmic values for the current density. Error bars  $\pm e_i$  of the fit parameters  $p_i$  are computed as  $e_i = (p_i^{(i)} - p_i^{(ii)})/2$ , where  $p_i^{(i)}$  and  $p_i^{(ii)}$  are the fit parameters of method (i) and (ii), respectively. It is known that an excessive alkali treatment

may lead to the formation of a barrier for the injection current in CIGS solar cells [46,47]. While all samples investigated in this study receive a heavy alkali PDT, no indication of a barrier, i.e., no distortion in the first quadrant of the *J-V* characteristics is observed, which could cause unreliable fitting results.

For two samples, the diode factor is additionally determined by  $J_{\text{SC}} - V_{\text{OC}}$  measurements obtained at different light intensities, where the diode factor is determined based on

$$\ln(-J_{\text{SC}}) = \ln J_0 + \frac{qV_{\text{OC}}}{A_{\text{el}} k_B T}, \quad (13)$$

where  $V_{\text{OC}}$  is the open-circuit voltage. Equation (13) is derived from Eq. (12) at  $V_{\text{OC}}$  and neglecting the shunt resistance. Note that the quantity  $-J_{\text{SC}}$  is positive. The diode factor is then obtained by a linear fit of  $\ln(-J_{\text{SC}})$  versus  $V_{\text{OC}}$ .

The FF of a *J-V* curve is given by

$$\text{FF} = \frac{V_{\text{MPP}} J_{\text{MPP}}}{V_{\text{OC}} J_{\text{SC}}} \quad (14)$$

where  $V_{\text{MPP}}$  and  $J_{\text{MPP}}$  are the voltage and current density at the maximum power point (MPP). In the one-diode model [Eq. (12)] the FF depends mainly on  $V_{\text{OC}}$  (Appendix G). To compare the FF for solar cells with different  $V_{\text{OC}}$  values, the FF is extracted from an artificial *J-V* curve [Eq. (12)] using the fit parameters of the (correct) one-diode fit, the  $J_{\text{SC}}$ , and an adjusted saturation current density  $J_{0,\text{fix}}$  according to

$$J_{0,\text{fix}} = \frac{-J_{\text{SC}} - (V_{\text{OC},\text{fix}}/R_{\text{sh}})}{\exp(qV_{\text{OC},\text{fix}}/A_{\text{el}} k_B T)}. \quad (15)$$

With the utilization of  $J_{0,\text{fix}}$  in Eq. (12), the resulting artificial *J-V* curve yields an open-circuit voltage of  $V_{\text{OC},\text{fix}}$ , keeping otherwise all parameters of the solar cell. For the comparison of the FF in this study, we use  $V_{\text{OC},\text{fix}} = 0.7$  V. Subsequently,  $\text{FF}_{\text{fix}}$  is extracted from the artificial *J-V* curve calculated using  $J_{0,\text{fix}}$ . It is noted that  $\text{FF}_{\text{fix}} \neq \text{FF}$ . However, this procedure allows the comparison of FFs from *J-V* curves with different  $V_{\text{OC}}$  values and takes into account non-negligible and individual contributions of parasitic resistances, which is not possible with previous empirical expressions [48].

## IV. RESULTS

### A. Epitaxial CIGS absorbers

For *p*-type CIGS,  $A > 1$  is due to a downshift of the hole quasi-Fermi-level in low-injection conditions. In the model of metastable defects [7] (see also Sec. II), electron injection converts metastable donors into acceptors. In contrast, in *n*-type CIGS films, electrons are majority carriers and

consequently exist abundantly compared to *p*-type CIGS. Within the same model, therefore, all metastable defects already exist in the acceptor configuration in equilibrium and do not change their state to a donor configuration upon excitation of the *n*-type CIGS layer. The reason is the dominating electron capture process ( $\tau_{EC}^{-1}$ ) due to the large number of free electrons and the small contribution from the hole capture process ( $\tau_{HC}^{-1}$ ) due to the scarcity of holes. Thus, a diode factor of 1 is expected.

Figure 3(a) shows the spectrally integrated PL flux as a function of the generation flux (linear to laser power) for the epitaxial absorber layers. The *n*-type CIGS samples with a GGI  $\leq 0.15$  are shown in blue, while *p*-type samples with GGI  $\geq 0.19$  are plotted in orange. Except for the sample with the highest PL flux, it is visible by eye that the *p*-type samples have a larger slope and therefore a higher diode factor [Eq. (1)] compared with the *n*-type samples. Linear fits are performed (dashed lines) and the diode factor (slope of the fit) is plotted in Fig. 3(b) versus the GGI. Clearly, a jump in the diode factor is observed at the transition between *n*-type and *p*-type CIGS. Also, *n*-type films have  $A = 1$  as expected for SRH recombination. A single *n*-type absorber exists with  $A > 1$  (gray dots and line in Fig. 3). This particular sample exhibits a much broader PL peak than the other samples and has the lowest CGI, as well as an increased contribution of an ordered defect compound, as seen from Raman spectroscopy [49] (Appendix H). We assume that in this sample the PL signal does not originate from a single-phase *n*-type Cu(In,Ga)Se<sub>2</sub>

absorber, which is the reason for the increased PL flux as well as the increased diode factor.

The results on epitaxial CIGS films support the model of metastable defects, as the *n*-type CIGS films show a diode factor of 1. In particular, the results demonstrate that bulk properties of *p*-type CIGS cause diode factors greater than 1 (see discussion at the beginning of this section), as grain boundaries are absent in epitaxial films and no alkalis are added in this study. Since all epitaxial samples are comparably thin, it can be expected that they are all similarly influenced by interface and surface recombination, no matter whether they are *p*-type or *n*-type. If one type of sample is more influenced by surface recombination, it is the *p*-type samples, which show generally lower PL flux. Thus, the influence of surface recombination can be excluded as the reason for the diode factor being equal to 1 in the *n*-type samples. We thus conclude that the observed change from  $A = 1$  to  $A > 1$ , as the conduction type changes from *n* to *p*, is due to the behavior of metastable defects, which are already in the acceptor state in equilibrium in the *n*-type films, whereas in *p*-type films they transition from donor state to acceptor state depending on the illumination.

## B. Polycrystalline CIGS absorbers

Four polycrystalline CIGS absorbers are investigated for the generation flux dependence of the diode factor. The *J-V* characteristics for the best solar cells fabricated from the same absorbers are shown in Appendix I. The solar cell parameters are summarized in Table IV. The generation flux dependence of the spectrally integrated PL flux for the polycrystalline CIGS samples is shown in Fig. 4(a). The differential diode factors [Eq. (1)] are plotted in Fig. 4(b) (solid symbols, dashed lines are added as a guide to the eye). Both samples with a PL peak position around 1.1 eV [inset of Fig. 4(a)] and without the addition of Ag, i.e., emission from a CuIn<sub>1-x</sub>Ga<sub>x</sub>Se<sub>2</sub> with  $x \approx 0.15$  (light blue and orange dots), show a slightly excitation-dependent diode factor: at 1-sun equivalent excitation (gray vertical line) the diode factor is approximately 1.3 and increases to 1.4 at lower generation fluxes. The sample with Ga located only towards the back contact (also without Ag) and a PL peak emission centered around 1.0 eV shows a rather constant diode factor of 1.4 (red dots). Interestingly, with the addition of Ag, i.e., a (Ag,Cu)(In,Ga)Se<sub>2</sub> absorber, the diode factor drops significantly to a value of approximately 1.1.

The model of metastable defects is employed to fit the experimental data. The result with the boundary condition of a minimum free-hole density in the dark of  $10^{14} \text{ cm}^{-3}$  is shown as solid lines in Fig. 4(b). The parameters for the fit are listed in Table II. Using the fitting parameters, the diode factor is additionally calculated outside the range of the experimental generation fluxes. The experimental data are missing in these regions because (i) the PL signal is

TABLE III. Parameters for the simulation of the diode factor. The free electron mass is denoted as  $m_e$ .

Parameters	Description	Value
$T$ (K)	Temperature	296
$E_g$ (eV)	Band gap	1.10
$N_A(\text{cm}^{-3})$	Doping density	$10^{16}$
$m_e^*$	Electron effective mass	$0.1 m_0$
$m_h^*$	Hole effective mass	$0.9 m_0$
$B(\text{cm}^3\text{s}^{-1})$	Radiative recombination constant	$1.28 \times 10^{-10}$
$\tau_{SRH}$ (ns)	Nonradiative lifetime for electrons and holes	100
$E_{t,SRH}$ (eV)	Distance of defect from the Valence band	0.6
$\Delta E_{EC}$ (eV)	Barrier for electron capture process	0.35
$\Delta E_{EE}$ (eV)	Barrier for electron emission process	Fit parameter
$\Delta E_{HC}$ (eV)	Barrier for hole capture process	Fit parameter
$\Delta E_{HE}$ (eV)	Barrier for hole emission process	Calculated [Eqs. (8) and (9)]
$N_{MS}(\text{cm}^{-3})$	Density of metastable defects	Fit parameter

TABLE IV. Solar cell parameters for the four polycrystalline CIGS devices investigated by PL spectroscopy (Fig. 4). For  $J-V$  curves see Appendix I.

Sample	Efficiency (%)	Fill factor (%)	$V_{OC}$ (V)	$J_{SC}$ (mAc $\text{cm}^{-2}$ )
ZSW	18.8	78.1	0.737	32.7
ZSW-Ag	18.1	81.0	0.703	31.8
AIST <sup>a</sup>	21.6	80.2	0.778	34.6
Empa <sup>a</sup>	19.2	74.5	0.609	42.3

<sup>a</sup>With antireflective coating.

too weak for lower generation fluxes, and (ii) the absorber layer can heat and influence the recombination dynamics for higher generation fluxes. The trend of the generation flux dependence and the magnitude of the diode factor are well described by the fits. In particular, for the ZSW, AIST, and Empa samples, the increased diode factors between 1.3 and 1.4 and the generation flux dependence are reproduced well. As elaborated in Sec. II (Theoretical Background), a generation-flux-independent diode factor of 1.1 over 4 orders of magnitude is more difficult to describe. Yet, this rather simple model can describe the observed diode factors between 1.4 and 1.1. It is interesting to note that the activation energies for the two very similar CIGS samples (ZSW and AIST) are the same within error. From the fit parameters in Table II, we see that  $\Delta E_{HC}$  for the Ag-containing sample is higher, indicating that the presence of Ag in the crystal changes the dynamics of this metastable defect. In particular, Ag makes the acceptor-to-donor transition slower. For the Empa sample, a considerably better fit is obtained when the boundary condition is relaxed to  $p_{0,\text{bound}} = 10^{13} \text{ cm}^{-3}$ , which is depicted in Fig. 4(b) as the light red curve. In particular, the improved fit with  $p_{0,\text{bound}} = 10^{13} \text{ cm}^{-3}$  results in considerably lower  $\Delta E_{HC}$  and  $\Delta E_{EE}$  values for the CuInSe<sub>2</sub> sample (Empa), indicating an even stronger influence of the Ga content. This observation is not unexpected, since the dynamics of the defect depends on the dynamics of the group-III dimer near the Se vacancy [50]. An overview of the fit quality ( $X^2$  values) and the energetic barriers  $\Delta E_{HC}$  and  $\Delta E_{EE}$  with the dependence on the fit boundary condition can be found in Appendix J.

## V. DISCUSSION

CIGS as used in solar cells is a *p*-type semiconductor with net *p*-type doping levels around  $10^{15}$  to  $10^{16} \text{ cm}^{-3}$  [10,11]. Using a carrier lifetime of  $\tau = 100 \text{ ns}$ , an absorber thickness  $d = 2 \mu\text{m}$ , and Eq. (6), the excess carrier density  $\Delta n$  is estimated to be  $10^{14} \text{ cm}^{-3}$  at 1-sun equivalent generation flux and as low as  $5 \times 10^{10}$  for a generation flux of  $10^{14} \text{ cm}^{-2} \text{ s}^{-1}$  (see also Appendix D). Clearly, the absorber is in low injection for the experimental conditions of the PL measurements. Thus, a diode factor of 1 is

expected without metastable defects for recombination in the quasineutral region, i.e., in the absence of a *p-n* junction [51]. The fact that the model of metastable defects [7] can describe the diode factor of  $A \approx 1.4$  for generation fluxes as low as  $10^{14} \text{ cm}^{-2} \text{ s}^{-1}$  supports the validity of this model.

The parameters for the fits shown in Fig. 4(b) dictate that the free-hole density in the dark, i.e., sufficiently low generation fluxes, is rather low, between  $10^{13}$  and  $10^{14} \text{ cm}^{-3}$ . This finding contradicts results obtained from other techniques such as capacitance-voltage profiling [11,40], electron-beam-induced current [52], or Hall [10,44,53] measurements, which report values around  $10^{15}$  and  $10^{16} \text{ cm}^{-3}$  [11]. Appendix J shows the fit to the experimental diode factors and the free-hole density with various boundary conditions up to  $p_{0,\text{bound}} = 10^{15} \text{ cm}^{-3}$ . Even though the quality of the fit deteriorates somewhat, it is still interesting to note that a qualitative agreement is found. At this point it is also stressed that only a very simple model is used here, i.e., a homogenous absorber (without band-gap grading), a single SRH recombination channel in the bulk of the absorber, no surface recombination, and only a single metastable defect. To give more details on one of these points, all samples employ an intentional GGI depth profile to increase charge-carrier collection and suppress surface recombination. An increasing GGI concentration increases the band gap by shifting up the conduction band [54]. Thus, the free-electron concentration is decreased at positions with higher GGI, which results in a smaller

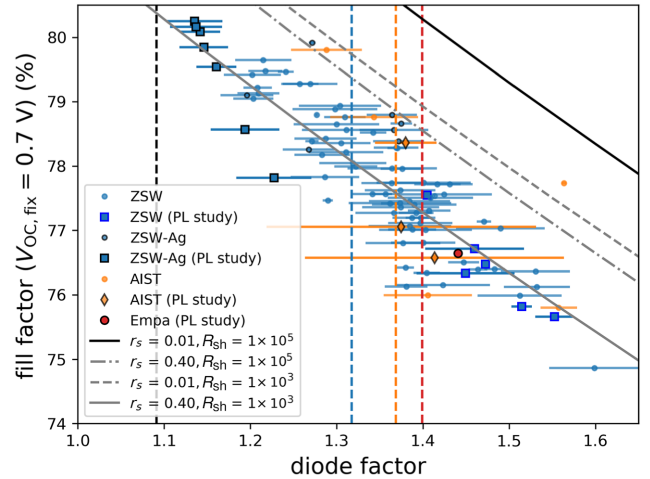


FIG. 5. FFs of finished solar cell devices as a function of the electrical diode factor (symbols). Highlighted symbols correspond to solar cells from the same absorber as used for the measurement of the optical diode factor by PL spectroscopy. Dashed vertical lines show the mean optical diode factors computed by averaging over the generation-flux-dependent data [see also Fig. 4(b)]. Gray and black lines show simulated FF based on the one-diode model [Eq. (12)] with (gray lines) and without (black line) parasitic resistances (units of  $\Omega\text{cm}^2$ ).

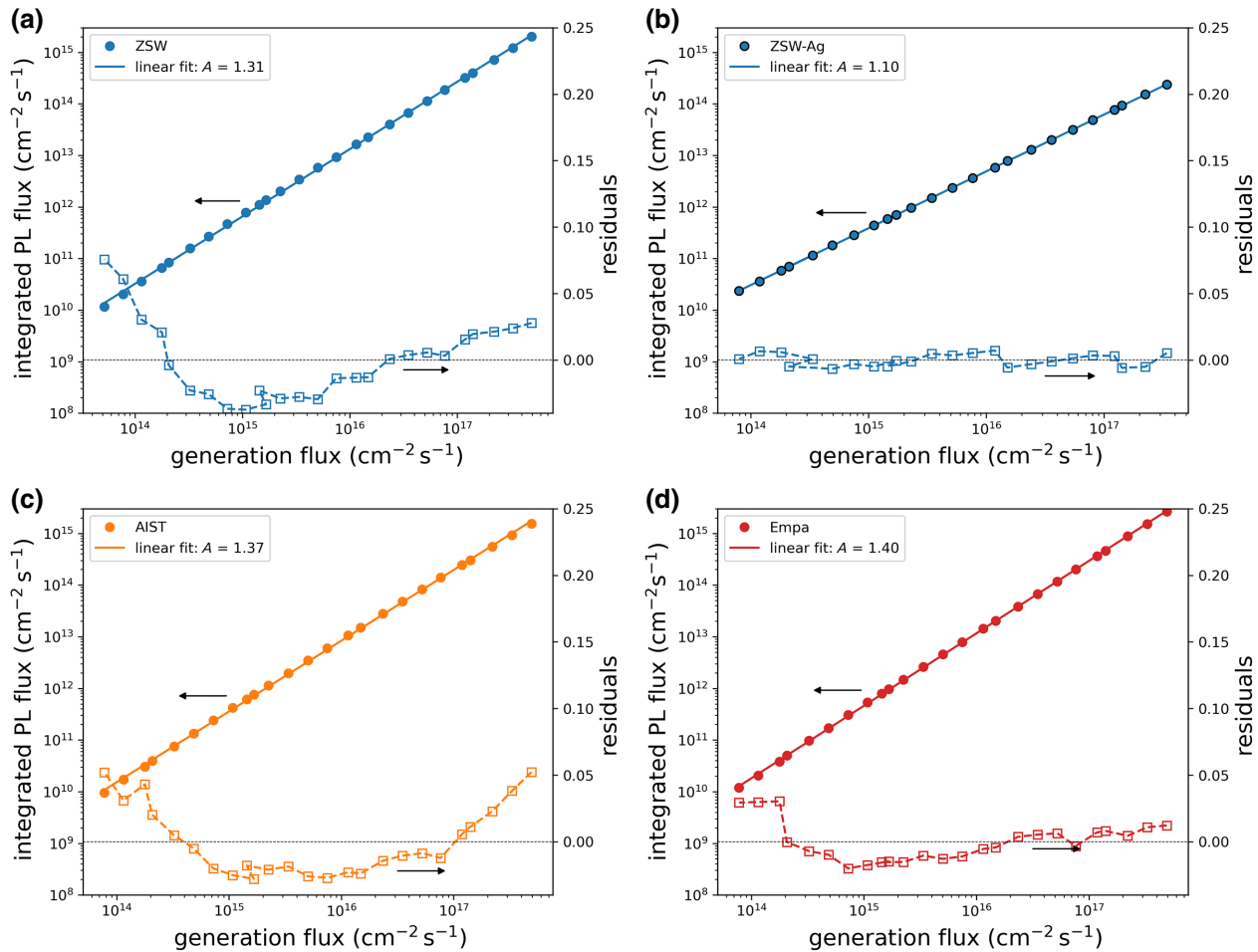


FIG. 6. Experimentally measured PL flux (filled symbols and left ordinate) as a function of the generation flux for the four investigated samples shown in Fig. 4, together with residuals of the fit (unfilled symbols and right ordinate).

fraction of metastable defects in the acceptor configuration compared with regions with lower GGI. In turn, the excitation dependence of the diode factor is smoothed out. Hence, it is possible that the poorer fit to the Ag-containing sample with  $A = 1.1$  is a result of the simplifications made previously.

In Refs. [55, 56], the authors present a voltage, i.e., generation flux, independent diode factor greater than 1 due to exponential defect distributions from the band edges into the band-gap region. However, these defect distributions only yield a diode factor greater than 1 for recombination where  $n = p$ , i.e., in the space-charge region, which is not the case for the material under investigation here. In particular, for a doped semiconductor under low-injection conditions and recombination in the quasineutral zone, as in a PL measurement, any defect distribution will result in a diode factor equal to 1 [51]. Furthermore, in these models, the diode factor remains at 2 in most cases; it is smaller than 2 only for tails with Urbach energies considerably larger than 25 meV ( $k_B$  at room temperature). Such tail states are not observed in CIGS absorbers [57].

Based on the discussion, one can ask if factors other than metastable defects may contribute to the increased diode factor (in low-injection conditions). A possible scenario might be the presence of space-charge regions (SCRs) within the absorber, possibly caused by the *n*-type doping of the CdS buffer layer [58] or charges located at grain boundaries. These SCRs could then result in regions where  $n \approx p$ . The diode factor is then influenced by high-injection conditions in these regions. However, we disregard this explanation due to the following points:

(i) A small SCR results only in a small band bending of the conduction and valence bands. Thus, in low-injection conditions, here for generation fluxes  $< 10^{-3}$  equivalent suns, electrons are still minority carriers. Thus, even though SCRs exist, the absorber layer is in a low-injection condition everywhere and a diode factor of 1 is expected for SRH recombination.

(ii) Large SCRs would result in charge-carrier separation effects. These effects can be observed well by time-resolved PL measurements and are evidenced by strongly

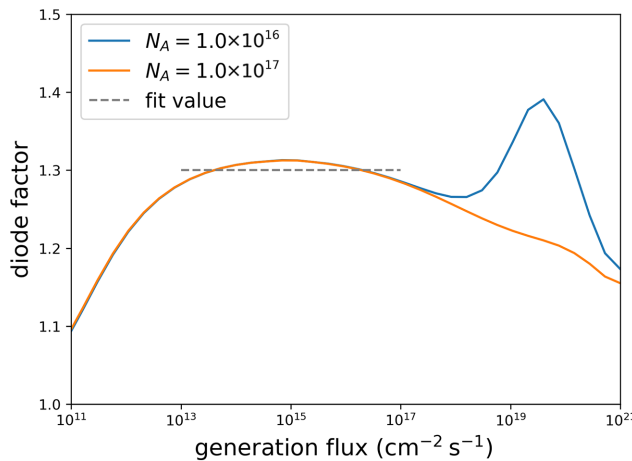


FIG. 7. Comparison of the fitted diode factors (solid lines) using different doping densities. As described in Sec. II, the doping density is a fixed parameter, while the metastable defect density is allowed to vary. The main difference occurs outside the experimentally accessible range of generation fluxes (otherwise heating of the sample needs to be taken into account) at generation fluxes greater than  $10^{18} \text{ cm}^{-2} \text{ s}^{-1}$ . The peak in the diode factor for  $N_A = 10^{16} \text{ cm}^{-2} \text{ s}^{-1}$  is due to high injection and dominating SRH recombination. The curve with  $N_A = 10^{17} \text{ cm}^{-2} \text{ s}^{-1}$  does not show this peak (or only as a shoulder at roughly 1 order of magnitude higher generation fluxes) because radiative recombination is already the dominating recombination channel.

reduced decay times of the transient [59]. However, CIGS absorber layers covered only with a CdS buffer layer generally do not exhibit such charge separation effects [59]. For instance, CuIn(Ga)Se<sub>2</sub> samples with a Ga grading only towards the back contact, similar to the Empa sample investigated here, show lifetimes as high as 400 ns

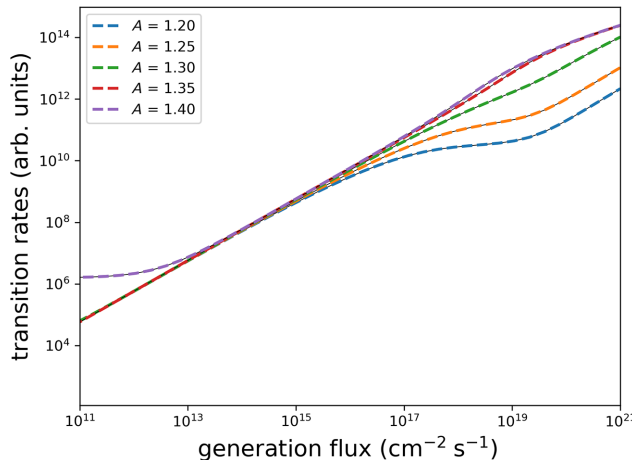


FIG. 8. Rates for the acceptor-to-donor (dashed colored lines) and donor-to-acceptor (black solid lines) transitions for the simulations presented in Fig. 2 of the main text (see Ref. [14] for details). Under steady-state conditions, these rates should be equal.

[36]. Furthermore, the existence of a SCR would lead to a reduced PL flux when measured over a small area (as is the case in our experiments). However, the PL flux of fresh absorbers before and after CdS deposition is the same [38].

(iii) The increased diode factor is also observed for *p*-type epitaxial absorber layers (Sec. IV A). These absorber layers are measured without a CdS buffer layer and do not incorporate grain boundaries.

Thus, we conclude that indeed the larger diode factors are due to an illumination-dependent doping density caused by metastable defects. Furthermore, recently we measured the doping density as a function of the light intensity in a light-soaking experiment by capacitance-voltage profiling [7]. It is found that the doping density increases with increasing light intensity, as expected for the model of metastable defects presented here. In particular, the increase of the doping density is in accordance with diode factors measured on the bare absorber layers.

It is interesting to note that the activation energy for the hole capture process  $\Delta E_{HC}$  is fitted to be higher for the Ag-containing CIGS sample (ZSW-Ag) compared with the Ag-free samples with similar band gaps (ZSW and AIST) as listed in Table II (see also Fig. 15b). The higher activation energy  $\Delta E_{HC}$  is evidenced complementarily by admittance spectroscopy measured on finished solar cell devices. Appendix K shows the measured capacitance as a function of the temperature in the relaxed and light-soaked states (see Ref. [7] for measurement details). The relaxation process happens for the Ag-containing CIGS sample at higher temperatures, which indicates a slower time constant and thus a higher activation energy  $\Delta E_{HC}$  for the

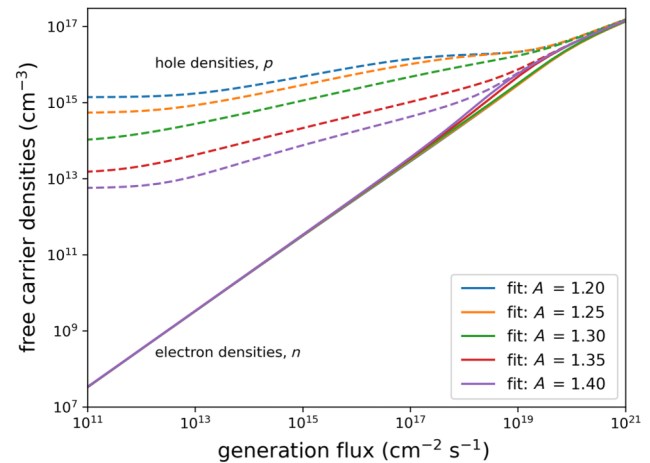


FIG. 9. Free-electron (solid lines) and hole (dashed lines) densities with respect to the generation flux for the fitted diode factors shown in Fig. 2(a). The fitting range is between  $10^{13}$  and  $10^{17} \text{ cm}^{-2} \text{ s}^{-1}$ . Clearly, within the fitting range and even slight above, the semiconductor is in low-injection conditions, i.e.,  $n \ll p$ .

hole capture process, which is mainly responsible for the acceptor-to-donor transition. It is stressed here that the values for the activation energies are not absolute as the activation energy for the electron capture process  $\Delta E_{EC}$  is fixed to 0.35 eV for the fitting routine. In order to obtain absolute values, dynamic measurements need to be carried out. Nevertheless, the activation energies can be compared relative to each other. It is found here that the activation energy for the hole capture process  $\Delta E_{HC}$  is smaller than the activation energy of the electron capture process  $\Delta E_{EC}$ . This trend, i.e.,  $\Delta E_{HC} < \Delta E_{EC}$ , is in contrast with values predicted theoretically [12] and used experimentally to model the doping profiles after voltage bias soaking from capacitance-voltage measurements [14]. To get a better understanding of the absolute values of the activation energies, dynamic measurements will be needed in combination with solutions of the time-dependent occupation function  $f_A$ . It is noteworthy, however, that in a previous study we found that the occupation of the metastable defect, i.e., the occupation function  $f_A$ , changes during an

$I$ - $V$  sweep and thus influences the diode factor of the  $I$ - $V$  characteristic [7].

To improve device efficiency, metastable defects responsible for the increased diode factors need to be avoided. Illuminated  $J$ - $V$  curves from a large set of samples from ZSW, AIST, and Empa are evaluated and the electrical diode factor is extracted from fitting (see Sec. III). Here, the electrical diode factor is distinguished from the diode factor measured optically and introduced previously (from now on labeled as the optical diode factor). The reason is that upon finishing the solar cell additional recombination channels might be introduced, which can lead to deviations of the electrical diode factor from the optical diode factor [8]. To reduce scattering of the data for the FF,  $J_0$  of the  $J$ - $V$  curves is scaled such that every curve yields  $V_{OC,fix} = 0.7$  V (see Sec. III). Figure 5 clearly shows that the FF increases as the electrical diode factor decreases. Assuming realistic values for the series and shunt resistance under illumination (Appendix L), the diode factor is the main contributor to the FF (gray solid line) according

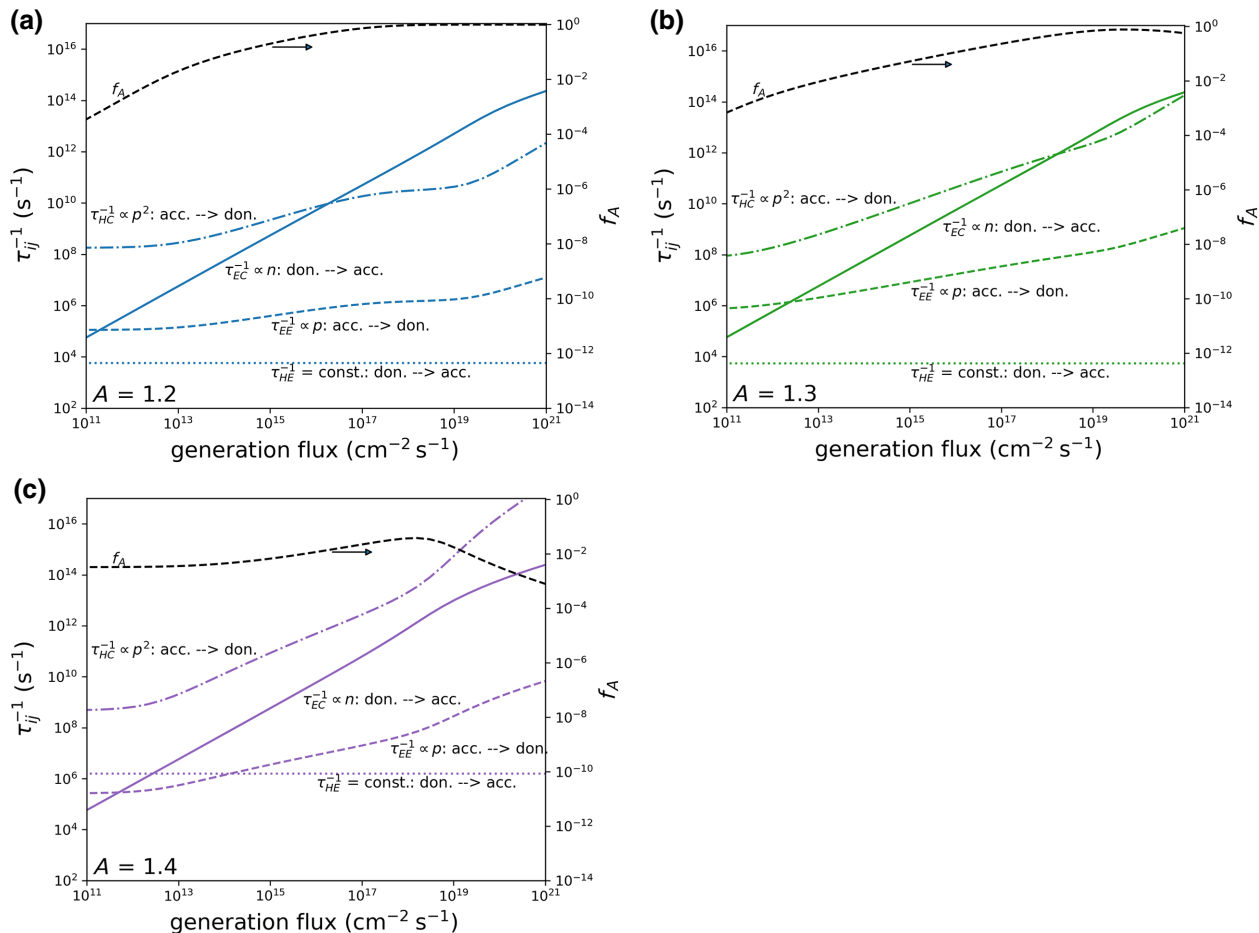


FIG. 10. Rate constants  $\tau_{ij}^{-1}$  for the four different transition processes (Table I) of the metastable defects between donor and acceptor state for the fits of an approximately constant diode factor of (a) 1.2, (b) 1.3, and (c) 1.4 [see Fig. 1(c)].

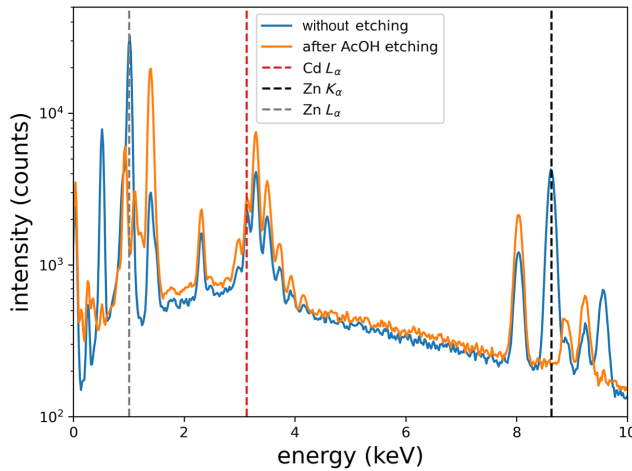


FIG. 11. Energy dispersive x-ray spectra for the Ag-containing solar cell prepared at ZSW before (blue) and after AcOH (orange) etching. As indicated by the gray and black dashed lines, the Zn signal is reduced below the detection limit, indicating that the AcOH etching removes the window layers with the Ni/Al grid fingers on top. However, the thin CdS buffer layer remains at the absorber surface as the Cd signal (red dashed line) is still detectable without any significant reduction in intensity.

to the one-diode model [Eq. (12)]. The simulated FFs demonstrate that the FF can be increased by 1% absolute if losses due to parasitic series or shunt resistances can be eliminated, respectively, or by 2% if both are eliminated. However, within the experimental range of diode factors the FF improves by more than 4%. Vertical dashed lines indicate the optical diode factors [Fig. 4(b)] averaged over all generation fluxes. The electrical diode factors

from the exact same pieces of absorbers are shown as the highlighted symbols (labeled “PL study”). In addition, for two of these samples (ZSW-Ag and Empa), the diode factors are determined by  $J_{SC}$  -  $V_{OC}$  measurements (Appendix M), which agree with the values shown in Fig. 5 determined by fitting the  $J$ - $V$  characteristics. It is apparent that the optical diode factors serve as a lower bound for the electrical diode factors. This behavior is expected when assuming additional SCR recombination taking place in a finished solar cell device, as SCR recombination has a diode factor close to 2 [51]. In addition, voltage-dependent carrier collection could lead to apparently increased fit values for the diode factor of the solar cells. In particular, the best solar cells (here from AIST), have electrical diode factors very close to the optical diode factor, while the deviations become larger for worse performing devices.

Notably, the addition of Ag during the CIGS deposition results in the lowest diode factors and consequently in the highest FFs of 81.0% at a  $V_{OC}$  of 703 mV for the best device (shown in Appendix I). With the addition of Ag, Essig *et al.* reported a 20.5% efficient device (with antireflective coating) with a high FF of 80.8% at a  $V_{OC}$  of 745 mV [32]. It is noted that this sample was prepared in the same deposition tool as the samples investigated here from ZSW. At the moment, it is not clear how Ag influences the electrical properties of the CIGS material and how the metastable defect density is influenced. In Ref. [60] (see Table I) the addition of Ag to CIGS also seems to improve the FF. However, the record reported device (20.9% efficiency) has a diode factor of 1.4 and only a FF of 76.8% at a  $V_{OC}$  of 814 mV. In contrast, in 2008 a CIGS solar cell prepared at NREL obtained a FF of 81.2% at a  $V_{OC}$  of only 690 mV; this solar cell was fabricated without Ag and without alkali PDT [61].

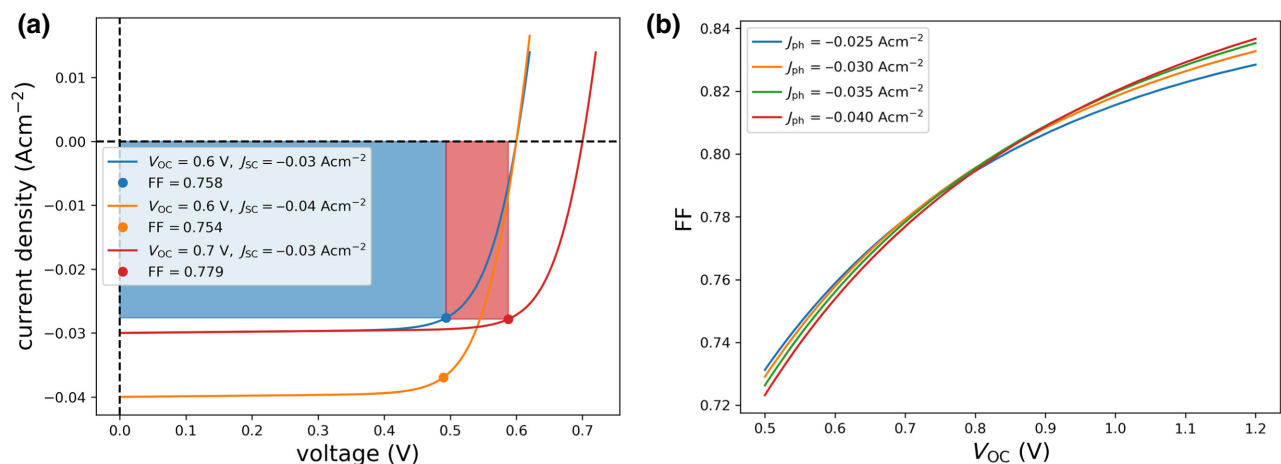


FIG. 12. (a) Simulated  $J$ - $V$  characteristics with fixed series and shunt resistances of 0.5 and  $1000 \Omega \text{cm}^2$  and a diode factor of 1.3. Solid circles indicate the maximum power point. The FF increases with  $V_{OC}$  as the portion of the rectangle takes a bigger contribution of the total area enclosed by the  $J$ - $V$  curve in the fourth quadrant. (b) Calculated FFs with respect to  $V_{OC}$  for different short-circuit current densities. Clearly,  $J_{SC}$  only has a minor effect on the FF.

Indeed, this particular sample had the lowest diode factor of 1.14 among the studied samples. Interestingly, one of the steps for improvements is described by an *in situ* high-temperature annealing at substrate growth temperature only in a Se atmosphere. Such an annealing could have an influence on the density of  $V_{\text{Cu}}-V_{\text{Se}}$  metastable defect complexes. Thus, at the moment it is not clear if Ag influences the metastable defect density directly or indirectly. Nevertheless, to obtain higher FF values, the diode factor needs to be reduced with the help of decreasing the influence of metastable defects.

## VI. CONCLUSION

The consequences of the  $V_{\text{Cu}}-V_{\text{Se}}$  metastable defect on the diode factor in Cu(In,Ga)Se<sub>2</sub> absorber layers and solar

cells is investigated. Because the  $V_{\text{Cu}}-V_{\text{Se}}$  changes from a donor to an acceptor state upon electron injection, the hole quasi-Fermi-level moves towards the valence band, which results in diode factors greater than 1, even in low-injection conditions. Using this model, we can explain:

(1) That *n*-type epitaxial Cu(In,Ga)Se<sub>2</sub> absorbers have a diode factor of 1 because electrons are majority carriers. Under these circumstances, all metastable defects already exist in the acceptor configuration in equilibrium and do not change their charge state upon the injection of holes.

(2) That *p*-type epitaxial Cu(In,Ga)Se<sub>2</sub> absorbers have a diode factor greater than 1 as expected in the presence of metastable defects. These results show that it is indeed an intrinsic bulk property of the Cu(In,Ga)Se<sub>2</sub> alloy.

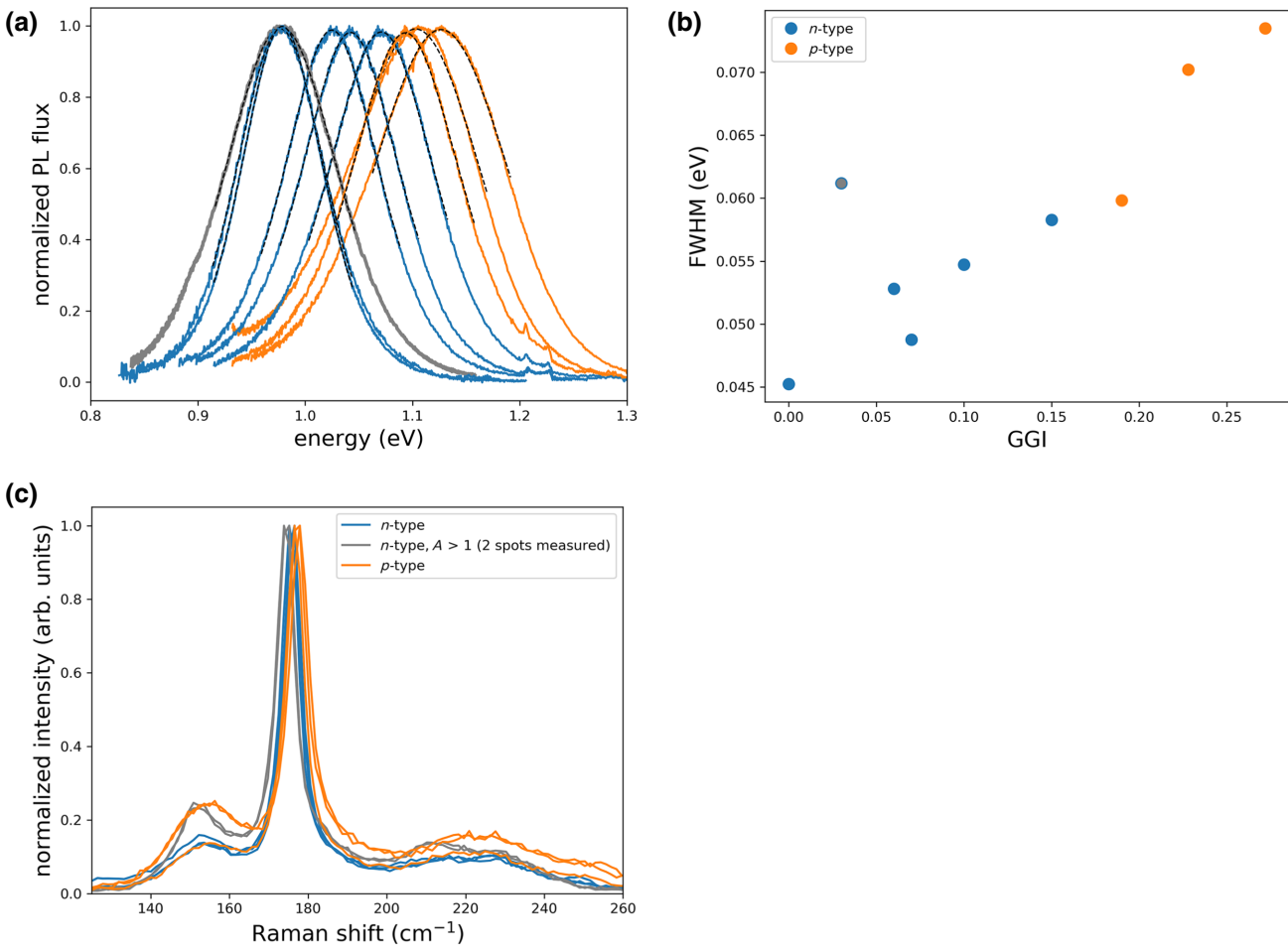


FIG. 13. (a) Normalized PL spectra for the epitaxial CIGS absorber layers presented in Fig. 3. Black dashed line is a fit using a pseudo-Voigt function to determine the FWHM. (b) Fitted FWHM for the PL spectra shown in (a). With increasing Ga content (GGI), the FWHM increases. This is expected, since the alloy disorder increases as the composition approaches GGI of 50%. However, the sample with GGI = 0.03 (gray data point), shows a significantly increased FWHM for its Ga content. This is the *n*-type sample with  $A > 1$ . (c) Raman spectra of the epitaxial CIGS layers. The *n*-type absorber with  $A > 1$  exhibits a strongly increased contribution at approximately 152–153 cm<sup>-1</sup> (determined by fitting with a double Lorentzian), which can be ascribed to the ordered defect compound like CuIn<sub>3</sub>Se<sub>5</sub> [49]. The strong peak a little bit below 180 cm<sup>-1</sup> corresponds to the  $A_1$  mode of CIGS and the small shifts are mainly induced by the different GGI ratios.

(3) The generation flux dependence (i.e., density of excess minorities) of the diode factor for high-quality polycrystalline Cu(In,Ga)Se<sub>2</sub> films. Experimentally, a small dependence of the diode factor with respect to the generation flux of the laser is measured, which can be well described by the model of the  $V_{\text{Cu}}-V_{\text{Se}}$  metastable defects.

In addition, we evaluate a large set of solar cells and their corresponding electrical diode factors from  $J-V$  characteristics. We find that the diode factor measured optically on the bare absorber imposes a lower limit for the electrical diode factor as measured on complete solar cells. In addition, a clear trend is observed regarding the effect of the diode factor on the FF: lower diode factors lead to higher FFs. Interestingly, absorber layers alloyed with Ag, i.e., (Ag,Cu)(In,Ga)Se<sub>2</sub>, demonstrate the lowest diode factors, which in turn lead to the highest FFs of 81.0%. We demonstrate that the dynamics and steady-state behavior of metastable defects depend on the composition of the sample. They increase the diode factor and thus reduce the FF and the efficiency.

### ACKNOWLEDGMENTS

This work was supported by the Luxembourgish Fond National de la Recherche in the framework of Project No. C17/MS/11696002 GRISC and by the German Federal Ministry for Economic Affairs and Climate Action (BMWK) within the EFFCIS-II and ODINCIGS projects under Contracts No. 03EE1059A and No. 03EE1078, respectively. The authors thank Ricardo Poeira for his assistance with the Raman measurements.

### APPENDIX A: CONSTANT DIODE FACTOR FIT TO EXPERIMENTAL DATA

When fitting experimental PL data often a single linear fit in the log-log plot is used. Figure 6 shows these fits for the samples considered here. The residuals (besides the one for the Ag-alloyed sample, ZSW-Ag) show a U-shaped residual, indicating that the diode factor is indeed slightly dependent on the excitation flux.

### APPENDIX B: ALTERNATIVE FIT FOR ANOTHER DOPING DENSITY

For the fits in Figs. 2 and 4 we fix the nonmetastable doping density  $N_A$ . Here we demonstrate that this is not critical for the fit in the experimentally accessible range (Fig. 7).

### APPENDIX C: STEADY-STATE CONDITIONS

Metastable defects often cause transient states; however, we consider a steady-state situation for each generation flux. Experimentally this is ensured by sufficiently slowing

the generation rate change. Furthermore, the same diode factor is obtained by reversing the scan direction in the excitation-dependent PL measurement, i.e., increasing or decreasing the generation flux. Steady state in simulations is ensured by equal backward and forward rates of the metastable transition, as demonstrated in Fig. 8.

### APPENDIX D: LOW INJECTION

Low-injection conditions are maintained as long as the density of photogenerated minorities is well below the majority doping level. Figure 9 confirms that this is the case in our simulations for excitation densities below  $3 \times 10^{17} \text{ cm}^{-2} \text{ s}^{-1}$  (in the worst case).

### APPENDIX E: ADDITIONAL DISCUSSION ON THE RATE CONSTANTS $\tau_{ij}^{-1}$

The rate constants  $\tau_{ij}^{-1}$  as a function of the generation flux are shown in Fig. 10 for the cases where the parameters of the metastable defect are fitted to yield diode factors of  $A = 1.2$ ,  $A = 1.3$ , and  $A = 1.4$ .

#### $A = 1.3$

The rate constants  $\tau_{EC}^{-1}$ ,  $\tau_{EE}^{-1}$ , and  $\tau_{HC}^{-1}$  vary as a power law (linear on log-log scale) over a wide range of generation fluxes. The steadily increasing contribution of  $\tau_{EC}^{-1} \propto n \propto G$  leads to a conversion of metastable defects into the acceptor state. Owing to that increase in the net doping density,  $\tau_{HC}^{-1}$  and  $\tau_{EE}^{-1}$  also increase until they level off between generation fluxes of  $10^{17}$  and  $10^{18} \text{ cm}^{-2} \text{ s}^{-1}$ , where  $f_A$  converges to 1. Thus, the diode factor is increased

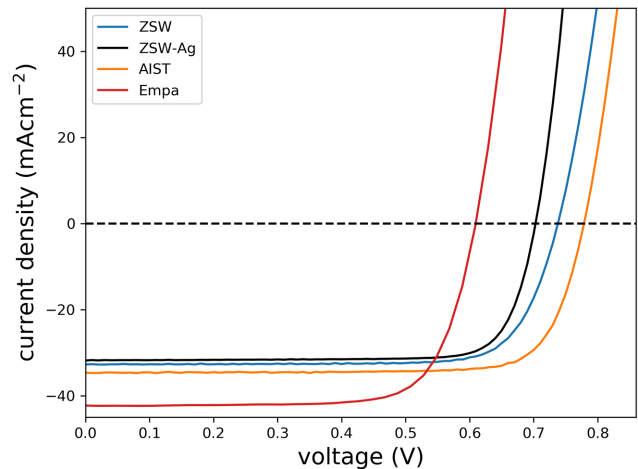


FIG. 14. Best  $J-V$  curves from the samples, which are used for the study of the diode factor by photoluminescence spectroscopy. The sample from AIST and Empa have an antireflection coating. The solar cell parameters are summarized in Table IV. The Empa sample has a lower band gap; it is a CuInSe<sub>2</sub> absorber with a Ga gradient only towards the back.

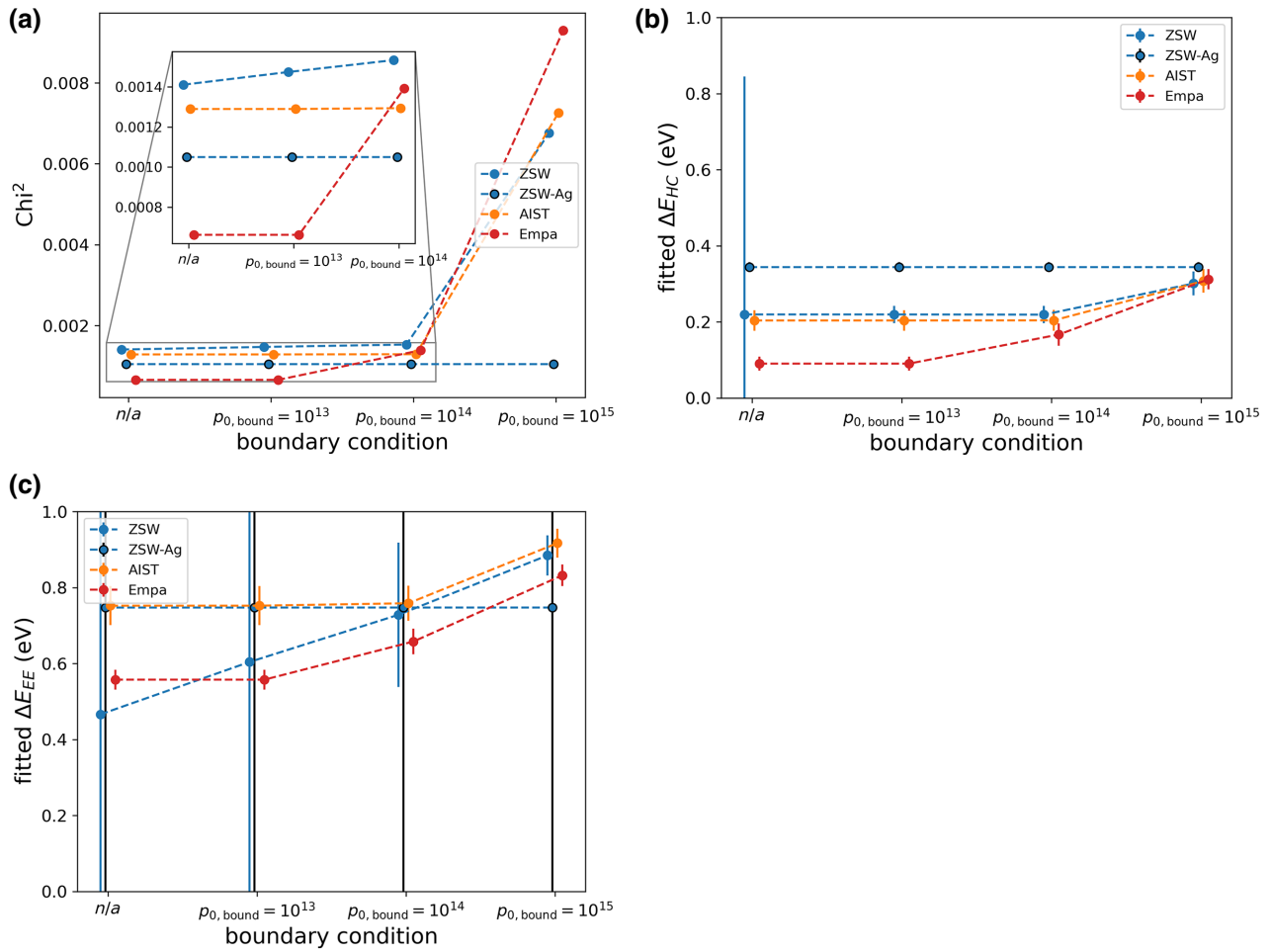


FIG. 15. (a) Quality of the fit for the four polycrystalline CIGS samples (see Fig. 4 and Table II) as a function of the boundary conditions. The three samples containing Ga throughout the whole absorber film and exhibiting emission peaks around 1.10–1.15 eV (ZSW, ZSW-Ag, AIST) demonstrate no significant deterioration of the fit quality for the boundary conditions up to  $p_0, \text{bound} = 10^{14} \text{ cm}^{-3}$ . The Empa sample, where Ga is only located towards the back contact, already shows an increased  $\chi^2$  of a factor of 2 for  $p_0, \text{bound} = 10^{14} \text{ cm}^{-3}$ . For  $p_0, \text{bound} = 10^{15} \text{ cm}^{-3}$ , the fit quality deteriorates for all samples with a “high” diode factor between 1.3 and 1.4. The fit for ZSW-Ag is not impeded by this condition as the best fit already results in a free-hole density of  $p_0 \approx 6 \times 10^{15} \text{ cm}^{-3}$ . (b),(c) Fitted values for the activation energy of the hole capture process  $\Delta E_{HC}$  and the electron emission process  $\Delta E_{EE}$ . Note that the activation energy for the electron capture process is fixed to  $\Delta E_{EC} = 0.35 \text{ eV}$ . Error bars are calculated from the covariance matrix of the fit result. The error bar for  $\Delta E_{EE}$  is generally rather large, which indicates that the diode factor is not very sensitive to this parameter. This is a consequence of the rather large values for this energy barrier, which results in a small rate constant  $\tau_{EE}^{-1}$  (see Appendix E) and thus in a small contribution to the transition from the metastable acceptor to donor state.

over a broad range of generation fluxes. For generation fluxes greater than  $10^{19} \text{ cm}^{-2} \text{ s}^{-1}$ , the system is in high-injection conditions resulting in a stronger increase of  $\tau_{HC}^{-1}$  and  $\tau_{EE}^{-1}$  as photogenerated holes significantly contribute to the hole density in the valence band.

### A = 1.2

Compared with the case of  $A = 1.3$ , the free-hole density for the lowest generation flux is higher (see Fig. 9). Consequently, the hole quasi-Fermi-level is closer to the valence band. Thus, the conversion of the metastable

defects from donor to acceptor results in a smaller shift of the hole quasi-Fermi-level and therefore in a smaller diode factor. For the lowest generation fluxes, the hole capture process (time constant  $\tau_{HC}^{-1}$ ) also dominates in the case of  $A = 1.2$ . Thus, to have the transition from the metastable donor to the acceptor in the same range of generation fluxes between  $10^{13}$  and  $10^{17} \text{ cm}^{-2} \text{ s}^{-1}$ , the activation energy for the hole capture needs to be higher (compared in Table II). For generation fluxes greater than around  $10^{17} \text{ cm}^{-2} \text{ s}^{-1}$ , almost all metastable defects are in the acceptor configurations and the diode factor decreases again towards 1.

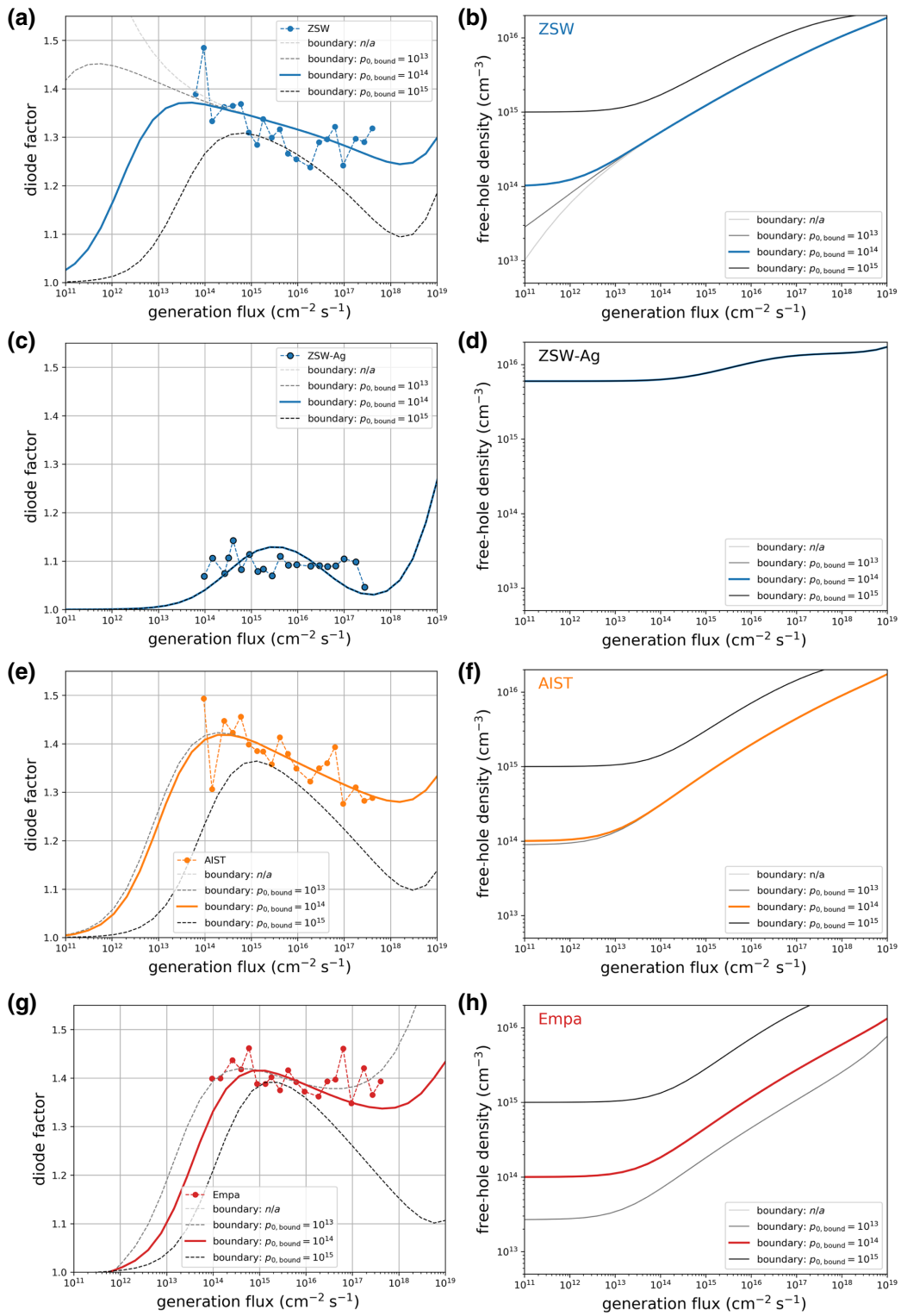


FIG. 16. Generation flux dependence of the diode factors measured by PL with fits using the model of metastable defects (a),(c),(e),(g) for the four polycrystalline CIGS absorbers (see Fig. 4 and Table II). Different boundary conditions are chosen to ensure a minimum free-hole density in the dark (i.e., lowest generation fluxes). The respective generation flux dependence of the free-hole density is shown in (b),(d),(f),(h). The most stringent boundary of  $p_0, \text{bound} = 10^{15} \text{ cm}^{-3}$  clearly deteriorates the quality of the fit (see also Fig. 10 for the  $X^2$  values). Nevertheless, the model is still able to describe the different diode factors. It is noted that only a very simple model is used, i.e., a homogeneous absorber without any band-gap gradient, a homogeneously distributed single SRH midgap recombination center without surface recombination, and a single homogeneously distributed metastable defect.

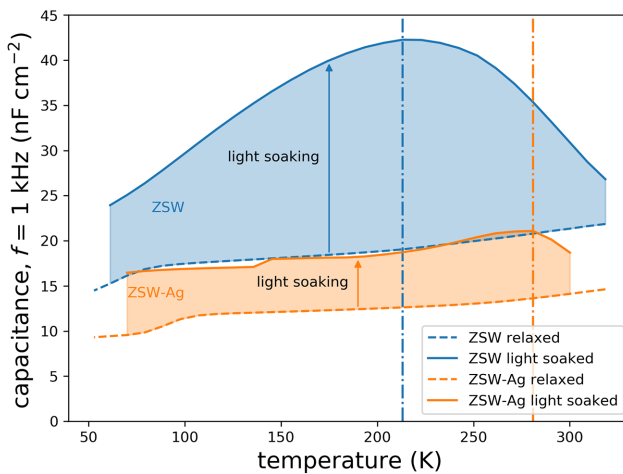


FIG. 17. Temperature dependence of the capacitance at an ac frequency of 1 kHz measured from low to high temperatures. In the relaxed state (dashed lines), the capacitance continuously increases with increasing temperature. In the light-soaked state, an increased capacitance is observed due to an increased doping density. The capacitance reaches a maximum value at a certain temperature (vertical dash dotted lines). For higher temperatures, the capacitance decreases in the light-soaked state, which is attributed to the relaxation of the metastable acceptors into the donor state. For the sample including Ag, this transition is at significantly higher temperatures, which agrees with the higher activation energy  $\Delta E_{HC}$  of the hole capture process as determined from the fits of the diode factor (Fig. 4 and Table II).

#### $A = 1.4$

Compared with the case of  $A = 1.3$ , the free-hole density for the lowest generation fluxes is lower (see Fig. 9), which allows for a greater shift of the hole quasi-Fermi-level and thus a larger diode factor. With increasing generation flux, the electron density increases, which results in small changes of the occupation of the metastable defects in the

acceptor state ( $f_A$  in Fig. 10). Owing to the low hole density, a small change in  $f_A$  results in a considerable shift of the hole quasi-Fermi-level, resulting in a diode factor of approximately 1.4. It is interesting to note that in this case,  $f_A$  never approaches 1. For generation fluxes greater than around  $10^{19} \text{ cm}^{-2}\text{s}^{-1}$ , the semiconductor is in high injection and therefore the occupation of  $f_A$  shifts towards 0 (see explanation for the case of  $A = 1.3$ ).

The simulations presented here show that the model of metastable defects [Eq. (5)] can describe very well a generation-flux-independent diode factor of 1.30–1.35. For diode factors outside this range, small deviations are expected, such as concave or convex shapes with respect to the generation flux.

## APPENDIX F: CdS LAYER AFTER ETCHING

The sample ZSW-Ag is only available as a complete solar cell. To make it comparable with the other absorber layers, the window is removed by etching in acetic acid, which leaves the CdS layer intact (Fig. 11).

## APPENDIX G: FILL FACTOR DEPENDENCE

We present simulations that study the dependence of the FF on  $J_{SC}$  and  $V_{OC}$  (Fig. 12).

## APPENDIX H: RAMAN SPECTROSCOPY

A single  $n$ -type sample in Fig. 3 shows a diode factor  $>1$ . This sample is different from the other  $n$ -type samples in various ways (Fig. 13).

## APPENDIX I: J-V CHARACTERISTIC OF SOLAR CELLS

The  $J$ - $V$  characteristics of the four discussed solar cells are shown in (Figure 14).

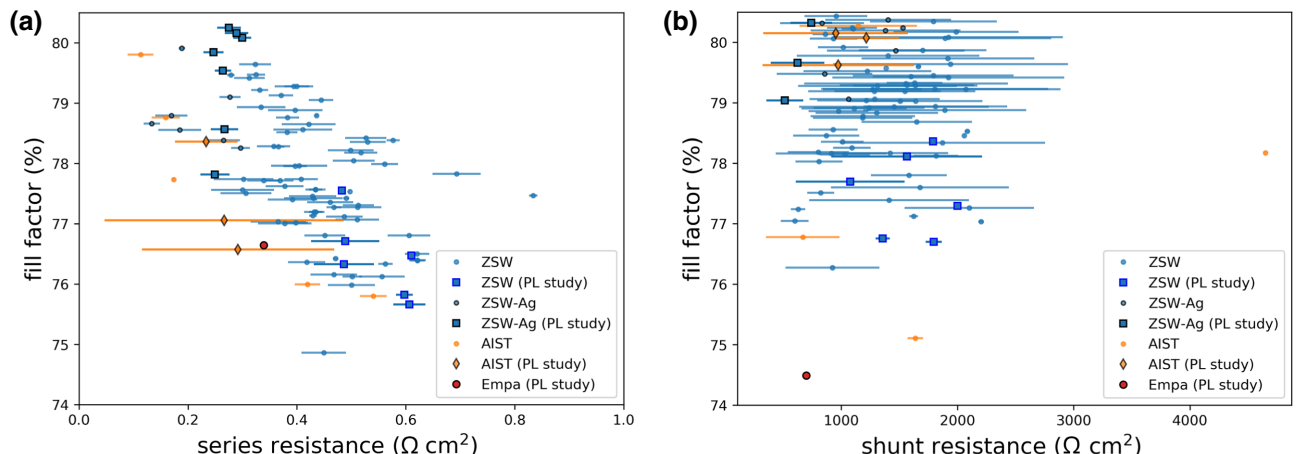


FIG. 18. Dependence of the FF with respect to the (a) series and (b) shunt resistance, extracted with the one-diode model from illuminated  $J$ - $V$  curves.

## APPENDIX J: DETAILED DISCUSSION OF THE DIODE FACTOR FITS

Here, we discuss the criticality of the boundary value of the dark hole concentration on the fit parameters (Figs. 15 and 16).

## APPENDIX K: RELAXATION OF LIGHT-SOAKING EFFECT

To get an indication of the differences in  $\Delta E_{HC}$ , we measure temperature-dependent capacitance. In the relaxed state the sample is relaxed at a temperature slightly above room temperature in the dark overnight, then cooled down and the capacitance measured as the temperature is increased. Light-soaked samples are illuminated at room temperature and cooled down under illumination. Then the capacitance measured as the temperature is increased. For more details, see Ref. [7] (Fig. 17).

## APPENDIX L: FF DEPENDENCE ON PARASITIC RESISTANCES

Figure 18 shows how the FF depends on the parasitic resistances.

## APPENDIX M: $J_{SC}$ VERSUS $V_{OC}$ MEASUREMENTS

Figure 19 shows  $J_{SC}$  vs.  $V_{OC}$  measurements of the samples ZSW-Ag and Empa.

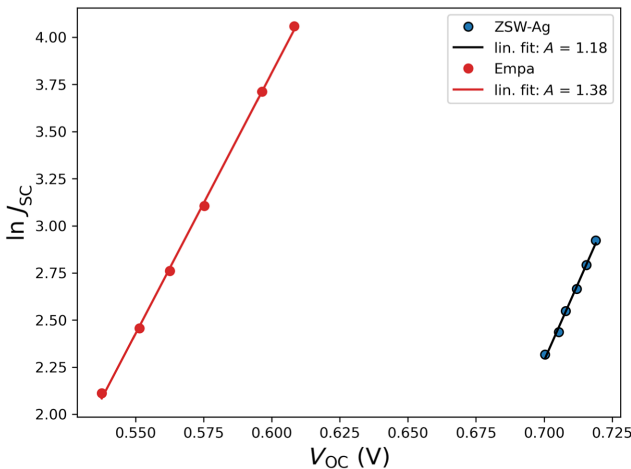


FIG. 19.  $J_{SC}$ - $V_{OC}$  measurement for the ZSW-Ag and Empa sample with the lowest and highest diode factors, respectively, where the generation-flux-dependent diode factor is determined by PL (see Fig. 4). The values obtained for the diode factor are in good agreement with the values obtained by fitting the  $J$ - $V$  characteristics (see Fig. 5).

- [1] M. Nakamura, K. Yamaguchi, Y. Kimoto, Y. Yasaki, T. Kato, and H. Sugimoto, Cd-free Cu(In,Ga)(Se,S)<sub>2</sub> thin-film solar cell with record efficiency of 23.35%, *IEEE J. Photovoltaics* **9**, 1863 (2019).
- [2] S. Siebentritt, *et al.*, Heavy alkali treatment of Cu(In,Ga)Se<sub>2</sub> solar cells: Surface versus bulk effects, *Adv. Energy Mater.* **10**, 1903752 (2020).
- [3] M. Krause, A. Nikolaeva, M. Maiberg, P. Jackson, D. Hariskos, W. Witte, J. A. Márquez, S. Levchenko, T. Unold, R. Scheer, and D. Abou-Ras, Microscopic origins of performance losses in highly efficient Cu(In,Ga)Se<sub>2</sub> thin-film solar cells, *Nat. Commun.* **11**, 4189 (2020).
- [4] M. A. Green, E. D. Dunlop, J. Hohl-Ebinger, M. Yoshita, N. Kopidakis, and X. Hao, Solar cell efficiency tables (Version 58), *Prog. Photovoltaics* **29**, 657 (2021).
- [5] K. Yoshikawa, H. Kawasaki, W. Yoshida, T. Irie, K. Konishi, K. Nakano, T. Uto, D. Adachi, M. Kanematsu, H. Uzu, and K. Yamamoto, Silicon heterojunction solar cell with interdigitated back contacts for a photoconversion efficiency over 26%, *Nat. Energy* **2**, 17032 (2017).
- [6] P. Jackson, R. Wuerz, D. Hariskos, E. Lotter, W. Witte, and M. Powalla, Effects of heavy alkali elements in Cu(In,Ga)Se<sub>2</sub> solar cells with efficiencies up to 22.6%, *Phys. Status Solidi RRL* **10**, 583 (2016).
- [7] T. P. Weiss, F. Ehre, V. Serrano-Escalante, T. Wang, and S. Siebentritt, Understanding performance limitations of Cu(In,Ga)Se<sub>2</sub> solar cells due to metastable defects—A route toward higher efficiencies, *Solar RRL* **5**, 210063 (2021).
- [8] F. Babbe, L. Choubrac, and S. Siebentritt, The optical diode ideality factor enables fast screening of semiconductors for solar cells, *Solar RRL* **2**, 1800248 (2018).
- [9] T. Wang, F. Ehre, T. P. Weiss, B. Veith-Wolf, V. Titova, N. Valle, M. Melchiorre, O. Ramírez, J. Schmidt, and S. Siebentritt, Diode factor in solar cells with metastable defects and back contact recombination, *Adv. Energy Mater.* **n/a**, 2202076 (2022).
- [10] T. Meyer, F. Engelhardt, J. Parisi, and U. Rau, Spectral dependence and Hall effect of persistent photoconductivity in polycrystalline Cu(In,Ga)Se<sub>2</sub> thin films, *J. Appl. Phys.* **91**, 5093 (2002).
- [11] M. Igelson, M. Maciaszek, K. Macielak, A. Czudek, M. Edoff, and N. Barreau, Concentration of defects responsible for persistent photoconductivity in Cu(In,Ga)Se<sub>2</sub>: Dependence on material composition, *Thin Solid Films* **669**, 600 (2019).
- [12] S. Lany and A. Zunger, Light- and bias-induced metastabilities in Cu(In,Ga)Se<sub>2</sub> based solar cells caused by the (VSe-VCu) vacancy complex, *J. Appl. Phys.* **100**, 113725 (2006).
- [13] J. Bailey, G. Zapalac, and D. Poplavskyy, in *Conference Record of the IEEE Photovoltaic Specialists Conference* (2016), pp. 2135.
- [14] K. Decock, P. Zabierowski, and M. Burgelman, Modeling metastabilities in chalcopyrite-based thin film solar cells, *J. Appl. Phys.* **111**, 043703 (2012).
- [15] K. Macielak, M. Maciaszek, M. Igelson, P. Zabierowski, and N. Barreau, Persistent photoconductivity in polycrystalline Cu(In,Ga)Se<sub>2</sub> thin films: Experiment versus theoretical predictions, *IEEE J. Photovoltaics* **5**, 1206 (2015).

- [16] D. V. Lang and R. A. Logan, Large-Lattice-Relaxation Model for Persistent Photoconductivity in Compound Semiconductors, *Phys. Rev. Lett.* **39**, 635 (1977).
- [17] K. Bothe, R. Hezel, and J. Schmidt, Recombination-enhanced formation of the metastable boron–oxygen complex in crystalline silicon, *Appl. Phys. Lett.* **83**, 1125 (2003).
- [18] A. Nagaoka, D. Kuciauskas, and M. A. Scarpulla, Doping properties of cadmium-rich arsenic-doped CdTe single crystals: Evidence of metastable AX behavior, *Appl. Phys. Lett.* **111**, 232103 (2017).
- [19] I. Mosquera-Lois, S. R. Kavanagh, A. Walsh, and D. O. Scanlon, “Identifying the ground state structures of point defects in solids” arXiv (2022). [arXiv:2207.09862](https://arxiv.org/abs/2207.09862)
- [20] H. Neumann and R. D. Tomlinson, Relation between electrical properties and composition in CuInSe<sub>2</sub> single crystals, *Solar Cells* **28**, 301 (1990).
- [21] O. Ramirez, E. M. Lanzoni, T. P. Weiss, R. Poeira, R. Leturcq, A. Redinger, and S. Siebentritt, How much gallium do we need for a p-type Cu(In,Ga)Se<sub>2</sub>? *APL Mater.* **10**, 061108 (2022).
- [22] T. Trupke, R. A. Bardos, M. D. Abbott, and J. E. Cotter, Suns-photoluminescence: Contactless determination of current-voltage characteristics of silicon wafers, *Appl. Phys. Lett.* **87**, 093503 (2005).
- [23] P. Wurfel, The chemical potential of radiation, *J. Phys. C: Solid State Phys.* **15**, 3967 (1982).
- [24] P. Calado, D. Burkitt, J. Yao, J. Troughton, T. M. Watson, M. J. Carnie, A. M. Telford, B. C. O'Regan, J. Nelson, and P. R. F. Barnes, Identifying Dominant Recombination Mechanisms in Perovskite Solar Cells by Measuring the Transient Ideality Factor, *Phys. Rev. Appl.* **11**, 044005 (2019).
- [25] P. Caprioglio, M. Stolterfoht, C. M. Wolff, T. Unold, B. Rech, S. Albrecht, and D. Neher, On the relation between the open-circuit voltage and quasi-Fermi level splitting in efficient perovskite solar cells, *Adv. Energy Mater.* **9**, 1901631 (2019).
- [26] P. Caprioglio, C. M. Wolff, O. J. Sandberg, A. Armin, B. Rech, S. Albrecht, D. Neher, and M. Stolterfoht, On the origin of the ideality factor in perovskite solar cells, *Adv. Energy Mater.* **10**, 2000502 (2020).
- [27] D. Kuciauskas, J. Moseley, P. Šćajev, and D. Albin, Radiative efficiency and charge-carrier lifetimes and diffusion length in polycrystalline CdSeTe heterostructures, *Phys. Status Solidi RRL* **14**, 1900606 (2020).
- [28] R. Noufi, R. Axton, C. Herrington, and S. K. Deb, Electronic properties versus composition of thin films of CuInSe<sub>2</sub>, *Appl. Phys. Lett.* **45**, 668 (1984).
- [29] M. A. Contreras, J. Tuttle, A. Gabor, A. Tenant, K. Ramanathan, S. Asher, A. Franz, J. Keane, L. Wang, J. Scofield, and R. Noufi, in *Conference Record of the IEEE Photovoltaic Specialists Conference* (1994), pp. 68.
- [30] A. M. Gabor, J. R. Tuttle, D. S. Albin, M. A. Contreras, R. Noufi, and A. M. Hermann, High-efficiency CuIn<sub>x</sub>Ga<sub>1-x</sub>Se<sub>2</sub> solar cells made from (In<sub>x</sub>,Ga<sub>1-x</sub>)<sub>2</sub>Se<sub>3</sub> precursor films, *Appl. Phys. Lett.* **65**, 198 (1994).
- [31] A. Kanevce, S. Paetel, D. Hariskos, and T. Magorian Friedlmeier, Impact of RbF-PDT on Cu(In,Ga)Se<sub>2</sub> solar cells with CdS and Zn(O,S) buffer layers, *EPJ Photovoltaics* **11**, 8 (2020).
- [32] S. Essig, S. Paetel, T. M. Friedlmeier, and M. Powalla, Challenges in the deposition of (Ag,Cu)(In,Ga)Se<sub>2</sub> absorber layers for thin-film solar cells, *J. Phys.: Mater.* **4**, 024003 (2021).
- [33] M. H. Wolter, B. Bissig, E. Avancini, R. Carron, S. Buecheler, P. Jackson, and S. Siebentritt, Influence of sodium and rubidium postdeposition treatment on the quasi-Fermi level splitting of Cu(In,Ga)Se<sub>2</sub> thin films, *IEEE J. Photovoltaics* **8**, 1320 (2018).
- [34] J. Nishinaga, T. Koida, S. Ishizuka, Y. Kamikawa, H. Takahashi, M. Iioka, H. Higuchi, Y. Ueno, H. Shibata, and S. Niki, Effects of long-term heat-light soaking on Cu(In,Ga)Se<sub>2</sub> solar cells with KF postdeposition treatment, *Appl. Phys. Express* **10**, 092301 (2017).
- [35] T. Feurer, B. Bissig, T. P. Weiss, R. Carron, E. Avancini, J. Löckinger, S. Buecheler, and A. N. Tiwari, Single-graded CIGS with narrow bandgap for tandem solar cells, *Sci. Technol. Adv. Mater.* **19**, 263 (2018).
- [36] T. Feurer, F. Fu, T. P. Weiss, E. Avancini, J. Löckinger, S. Buecheler, and A. N. Tiwari, RbF post deposition treatment for narrow bandgap Cu(In,Ga)Se<sub>2</sub> solar cells, *Thin Solid Films* **670**, 34 (2019).
- [37] D. Regesch, L. Gütay, J. K. Larsen, V. Deprédurand, D. Tanaka, Y. Aida, and S. Siebentritt, Degradation and passivation of CuInSe<sub>2</sub>, *Appl. Phys. Lett.* **101**, 112108 (2012).
- [38] F. Babbe, L. Choubrac, and S. Siebentritt, Quasi Fermi level splitting of Cu-rich and Cu-poor Cu(In,Ga)Se<sub>2</sub> absorber layers, *Appl. Phys. Lett.* **109**, 082105 (2016).
- [39] T. P. Weiss, B. Bissig, T. Feurer, R. Carron, S. Buecheler, and A. N. Tiwari, Bulk and surface recombination properties in thin film semiconductors with different surface treatments from time-resolved photoluminescence measurements, *Sci. Rep.* **9**, 5385 (2019).
- [40] F. Pianezzi, P. Reinhard, A. Chirilă, B. Bissig, S. Nishiwaki, S. Buecheler, and A. N. Tiwari, *Phys. Chem. Chem. Phys.* **2014**, 8843 (2014).
- [41] A. Czudek, A. Eslam, A. Urbaniak, P. Zabierowski, R. Wuerz, and M. Igelson, Evolution of the electrical characteristics of Cu(In,Ga)Se<sub>2</sub> devices with sodium content, *J. Appl. Phys.* **128**, 173102 (2020).
- [42] O. Ramírez, M. Bertrand, A. Debot, D. Siopa, N. Valle, J. Schmauch, M. Melchiorre, and S. Siebentritt, The effect of potassium fluoride postdeposition treatments on the optoelectronic properties of Cu(In,Ga)Se<sub>2</sub> single crystals, *Solar RRL* **5**, 2000727 (2021).
- [43] R. K. Ahrenkiel, *Semiconductors and Semimetals* (Academic Press, Boston, 1993), p. 39.
- [44] F. Werner, D. Colombara, M. Melchiorre, N. Valle, B. El Adib, C. Spindler, and S. Siebentritt, Doping mechanism in pure CuInSe<sub>2</sub>, *J. Appl. Phys.* **119**, 173103 (2016).
- [45] A. R. Burgers, J. A. Eikelboom, A. Schonecker, and W. C. Sinke, in *Conference Record of the IEEE Photovoltaic Specialists Conference* (1996), pp. 569.
- [46] T. P. Weiss, S. Nishiwaki, B. Bissig, R. Carron, E. Avancini, J. Löckinger, S. Buecheler, and A. N. Tiwari, Injection current barrier formation for RbF postdeposition-treated

- Cu(In,Ga)Se<sub>2</sub>-based solar cells, *Adv. Mater. Interfaces* **5**, 1701007 (2018).
- [47] F. Werner, M. H. Wolter, S. Siebentritt, G. Sozzi, S. Di Napoli, R. Menozzi, P. Jackson, and W. Witte, “Alkaline treatment of Cu(In,Ga)Se<sub>2</sub> thin film absorbers: transport barriers and their influence on the admittance spectrum” unpublished (2017).
- [48] M. A. Green, Solar cell fill factors: General graph and empirical expressions, *Solid-State Electron.* **24**, 788 (1981).
- [49] C.-M. Xu, X.-L. Xu, J. Xu, X.-J. Yang, J. Zuo, N. Kong, W.-H. Huang, and H.-T. Liu, Composition dependence of the Raman A 1 mode and additional mode in tetragonal Cu-In-Se thin films, *Semicond. Sci. Technol.* **19**, 1201 (2004).
- [50] S. Lany and A. Zunger, Metal-Dimer Atomic Reconstruction Leading to Deep Donor States of the Anion Vacancy in II-VI and Chalcopyrite Semiconductors, *Phys. Rev. Lett.* **93**, 156404 (2004).
- [51] R. Scheer and H. W. Schock, *Chalcogenide Photovoltaics: Physics, Technologies, and Thin Film Devices* (Wiley-VCH Verlag & Co. KGaA, Weinheim, Germany, 2011).
- [52] D. Abou-Ras, N. Schäfer, N. Baldaz, S. Brunken, and C. Boit, Electron-beam-induced current measurements with applied bias provide insight to locally resolved acceptor concentrations at *p-n* junctions, *AIP Adv.* **5**, 077191 (2015).
- [53] F. Werner, Hall measurements on low-mobility thin films, *J. Appl. Phys.* **122**, 135306 (2017).
- [54] A. Klein, Energy band alignment in chalcogenide thin film solar cells from photoelectron spectroscopy, *J. Phys.: Condens. Matter* **27**, 134201 (2015).
- [55] T. Walter, R. Herberholz, and H. W. Schock, Distribution of defects in polycrystalline chalcopyrite thin films, *Solid State Phenomena* **51-52**, 309 (1996).
- [56] C. van Berkel, M. J. Powell, A. R. Franklin, and I. D. French, Quality factor in *a-Si:H nip* and *pin* diodes, *J. Appl. Phys.* **73**, 5264 (1993).
- [57] M. H. Wolter, R. Carron, E. Avancini, B. Bissig, T. P. Weiss, S. Nishiwaki, T. Feurer, S. Buecheler, P. Jackson, W. Witte, and S. Siebentritt, How band tail recombination influences the open-circuit voltage of solar cells, *Prog. Photovoltaics* **30**, 702 (2022).
- [58] S. J. Heise and J. F. López Salas, Charge separation effects in time-resolved photoluminescence of Cu(In,Ga)Se<sub>2</sub> thin film solar cells, *Thin Solid Films* **633**, 35 (2017).
- [59] W. K. Metzger, I. L. Repins, M. Romero, P. Dippo, M. Contreras, R. Noufi, and D. Levi, Recombination kinetics and stability in polycrystalline Cu(In,Ga)Se<sub>2</sub> solar cells, *Thin Solid Films* **517**, 2360 (2009).
- [60] M. Edoff, T. Jarmar, N. S. Nilsson, E. Wallin, D. Högström, O. Stolt, O. Lundberg, W. Shafarman, and L. Stolt, High  $V_{oc}$  in (Cu,Ag)(In,Ga)Se<sub>2</sub> solar cells, *IEEE J. Photovoltaics* **7**, 1789 (2017).
- [61] I. Repins, M. A. Contreras, B. Egaas, C. DeHart, J. Scharf, C. L. Perkins, B. To, and R. Noufi, 19.9%-efficient ZnO/CdS/CuInGaSe<sub>2</sub> solar cell with 81.2% fill factor, *Prog. Photovoltaics* **16**, 235 (2008).